Department of the Faculty of Civil Engineering and Geosciences

Thermal Dispersion in Geothermal Doublets

Supervised by Bill Rossen and Alexandros Daniilidis

BSc thesis

Bart Bonhof
8-7-2022

Preface

I have written this report as a bachelor's thesis for the BSc Applied Earth Sciences of the TU Delft Faculty of Civil Engineering & Geosciences during the fourth quarter of my third year of university. During this time, I not only learned how to carry out a valid and reliable investigation, but also learned to work and deliberate my findings in a professional scientific setting. I am very grateful to have had the privilege of working with Bill Rossen and Alexandros Daniilidis as my supervisors. For the past few months, they have greatly inspired me to work on this project by constantly providing me with constructive feedback and all the help that I needed. Also, I want to thank Pelle van Nieuwkerk and Jinyu Tang for their contributions to the weekly discussions that we have had about this topic, and for allowing me to use their works. Because of all this, I can genuinely say that I have finished my thesis with immense joy and fulfilment.

Bart Bonhof

Delft, July 2022

Student number:	5057809
Project duration:	21 April 2022 – 8 July 2022
Thesis supervisors:	Prof. W.R. Rossen, TU Delft Prof. A.D. Daniilidis, TU Delft

Abstract

Heating from geothermal doublets might contribute to the adaptation from fossil energy into greener methods for a CO_2-neutral future. Recently, P. van Nieuwkerk (2022) has demonstrated how a new upscaling method developed by Tang et al. (2022) produces more accurate predictions of production temperature over time when an increase in the vertical thermal conductivity parameter (k_z) is implemented in simulations. The results of Van Nieuwkerk's research might be used in optimising geothermal doublet performance. This thesis explores whether a justified physical reason for increasing k_z exists. Concretely, this study compares analytical solutions and modelled solutions, based on a simplified layer-cake model, of a situation of conductive heat transfer for which analytical solutions already exist. A technique called superposition has been applied to both solutions in order to match the in situ situation more accurately. Results of the most realistic cases that have been investigated show that the modelled and analytical solutions do not vary considerably in temperature predictions over time. Therefore, this research has not identified any physical grounds that justify an increase in k_z. Nevertheless, since this report has only considered a simplified model that bears limited resemblance to the in situ situation, it does not mean that there is none. Based on these results, future research is necessary to make more specific evidentiary claims.

Table of Contents

1. Introduction

The end of the lifetime of a geothermal doublet is marked by a drop in production temperature of the well. When the water that the geothermal production well produces falls deeply below the original production temperature, the process becomes unviable and must end. As geothermal heat production requires substantial initial investments, it is of major importance to be able to make the most accurate possible predictions about the lifespan of a geothermal doublet (Milieu Centraal, 2020). With more accurate predictions of the performance of potential future geothermal doublets, governments and the industry will be able to better predict the most efficient location for potential geothermal doublets, thereby minimizing energy costs (Daniilidis et al., 2021). But since geological reservoirs are often very heterogeneous, modelling heat dissipation in geothermal doublets is computationally expensive (Voskov et al., 2019). To bypass this issue, simulators must use big heterogeneous grid blocks for functioning efficiently. Therefore, modelling geothermal doublet performance requires upscaling techniques. However, when using bigger grid blocks, there are concerns about accuracy. This thesis will address one of them.

Recently, J. Tang et al. (2022) have submitted to journal a paper that presents a new method that can be used to upscale rock conductivities in the flow direction of geothermal doublets. In research that is still in preparation, P. van Nieuwkerk (2022) has investigated whether Tang et al.'s new upscaling technique outperforms the conventional upscaling method when modelling the temperature development in geothermal doublets over time. To do so, Van Nieuwkerk performed fine-grid simulations on a reservoir and then compared its results to those obtained from the two upscaling methods. Results show that Tang et al.'s new upscaling technique produces results that resemble the fine-grid simulations more accurately than results obtained with conventional upscaling. However, Tang et al.'s upscaling results do not quantitatively fit the fine-grid simulation when predicting the initial drop in produced water temperature that is crucial to the closing of a project. Despite not having found any valid physical explanation, Van Nieuwkerk also discovered that increasing the vertical thermal conductivity parameter (k_z) resulted in a much better fit.

As no valid physical reason has yet been found, the aim of this thesis is to investigate whether increasing k_z is justified or if increasing the k_z value is just a cover for imperfections in upscaling techniques. This is done through considering a simplified model with a set of two alternating layers with identical properties, where only the initial temperatures of the two layers are different. In the model, both for simplicity and to allow comparisons with analytical solutions, the only heat transfer mechanism considered is conduction. Conduction in a heterogeneous reservoir is the mechanism that mitigates the spreading of the cold waterfront caused by forced convection taking place in the fast-moving flow layers (Tang et al., 2022).

The report is structured as follows. In Chapter 2, the theoretical knowledge behind this research will be provided. Chapter 3 will be about the methods used in this thesis, and Chapter 4 will present the results obtained in this thesis. Then, Chapter 5 will discuss limitations of this study. Finally, Chapter 6 will present the findings from this research.

2. Research background

2.1 Geothermal energy in the Netherlands

The world has a global -crisis on its hands. Of the 193 countries that have made a pledge under the Paris Agreement to half their greenhouse gas emissions by 2030, experts say that even if every country would abide by the plans that have been set forth, only thirty-six members would accomplish their vowed goals (Watson et al., 2019). In their report, Watson et al. warn that by 2030, the economic losses due to cataclysmic weather events caused by the failure of governments to constrict greenhouse gas emissions will be at a minimum of almost $2 billion dollars per day. One of the countries that is still not on track to achieve their part of the Paris Agreement is The Netherlands (Hammingh et al., 2020). To accomplish their climate goals, the Dutch would have to have reduced their CO_2 emissions by 95% by 2050, compared to 2015. It is for this reason that it is ever more crucial for the government in the Netherlands to explore and consider all means of greenhouse gas emission reductions.

40% of the CO_2 budget in the Netherlands is accounted for by heat consumption (EBN, 2018). To transition towards a CO_2 neutral form of heat generation, the Dutch government will minimize social costs by making use of a variety of renewable sources and techniques. One of the most promising methods of sustainable heat generation is the application of geothermal doublets. By 2050, geothermal energy is forecasted to contribute to 23% of the total Dutch heat production (EBN, 2018).

2.2 The principle behind geothermal doublets

A geothermal doublet produces energy by extracting heat from the Earth's hot subsurface. Figure 1 is a schematic representation of such a doublet. A geothermal doublet works by producing hot resident water and, after harvesting the heat, injecting the cooled down water back into an aquifer. A heat exchanger on the surface is used to extract the heat from the hot water. Eventually however, the cold temperature starts to break through to the production well, forcing the closure of the project. Even though geothermal doublets can be deployed as a very sustainable and reliable source of energy, as of now, very few geothermal doublets exist in the Netherlands (Dijkstra et al., 2020). The reason for this is that geothermal energy requires large upfront investments caused by expensive drilling operations. In the Netherlands, the main targets for geothermal doublets are at depths of between 2 and 2.5 km with a temperature between 70 and 90 °C (Bonté et al., 2012).

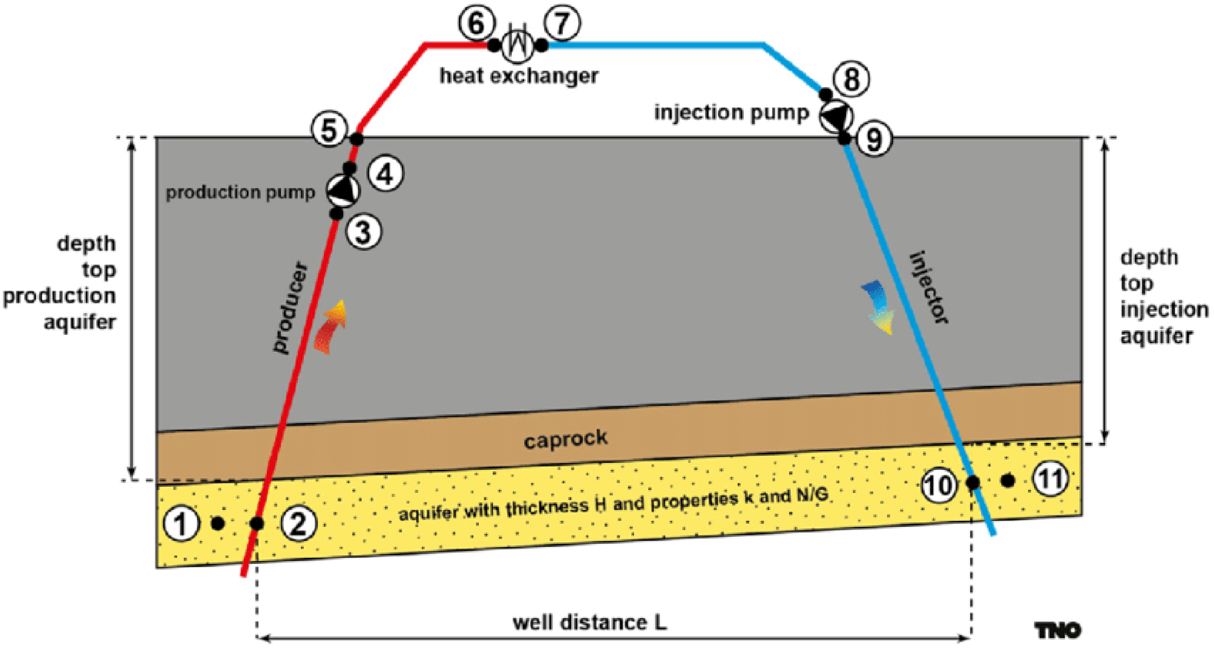

Figure 1. A schematic representation of a geothermal doublet (Mijnlieff, 2020)

2.3 The lifespan of a geothermal doublet

At the end of the lifespan of a geothermal doublet, the injected cold water has flowed through the reservoir rock long enough to cool down the reservoir until the water being produced gets too cold to be an economically viable process. The rate at which the production temperature of a geological doublet cools down is dependent on multiple aspects, including injection temperature, well spacing, flow rate, reservoir thickness, reservoir permeability and porosity, and the heterogeneity of the reservoir rock (Daniilidis et al., 2020; Wang et al., 2021). Typically, shutdown happens shortly after the first decline in temperature of the reservoir rock at the production well (Daniilidis et al., 2021). For most commercial doublets, the lifespan ranges anywhere from 25 to 40 years (Mahbaz et al., 2021).

The first significant drop in produced water temperature of geothermal doublets occurs when a cold-water temperature front has penetrated the reservoir rock surrounding the production well. In heterogeneous reservoirs, the reservoir will cool down quickest in the layers with the highest permeability. The reason for this is that layers of high permeability experience a significant increase in cold water flow rates. Consequently, higher rates of convection make the reservoir rock that surrounds the pathway of increased cold-water flow cool down quicker. This effect of increased thermal dispersion in the reservoir caused by variations in flow rates between geological layers is mitigated through conduction (Tang et al., 2022).

2.4 Modelling geothermal doublets

One method that can be used to bring down energy costs of geothermal doublets would be for operators to choose well locations with the longest cumulative lifespan production output. As subsurface information is limited, accurate modelling of doublet performance is key. The modelling of complex heterogeneous reservoirs, though, is very computationally inefficient. To solve this, upscaling techniques with big heterogeneous grid blocks are necessary (Tang et al., 2022).

Recently, J. Tang et al. (2022) have developed a new upscaling technique that can be used to upscale rock conductivities in the flow direction of geothermal doublets. This new upscaling technique has been assessed on a reservoir model by P. van Nieuwkerk. Figure 2 below shows the temperature distribution after 10 years of production generated by a fine-grid simulation of the reservoir model. Figure 3 displays the same situation, but now modelled with Tang et al.'s upscaling technique with just 12 layers. In his research that is still in preparation, P. van Nieuwkerk has found that Tang et al.'s new 'Taylor' upscaling technique outperforms the conventional 'arithmetic' upscaling method when modelling the temperature development in geothermal wells over time.

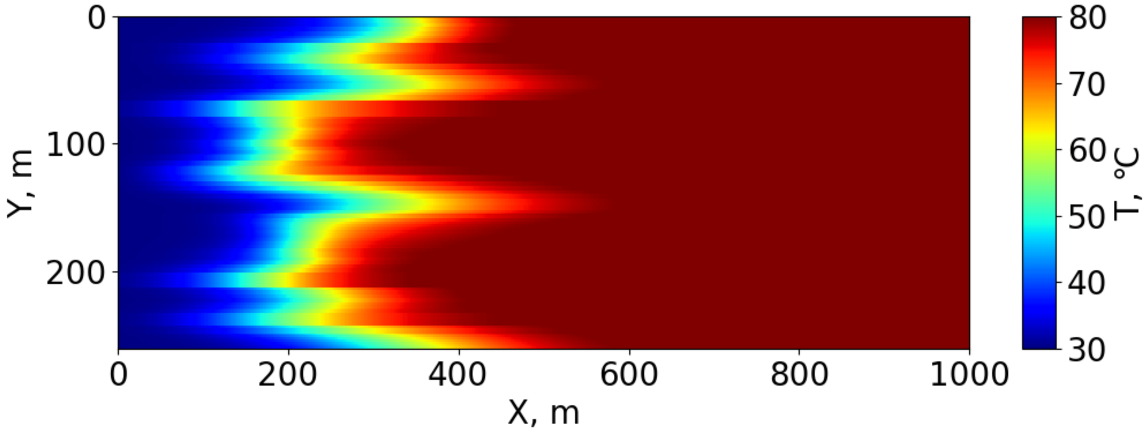

Figure 2. An example of a fine-grid simulation after 10 years of production (Van Nieuwkerk, 2022)

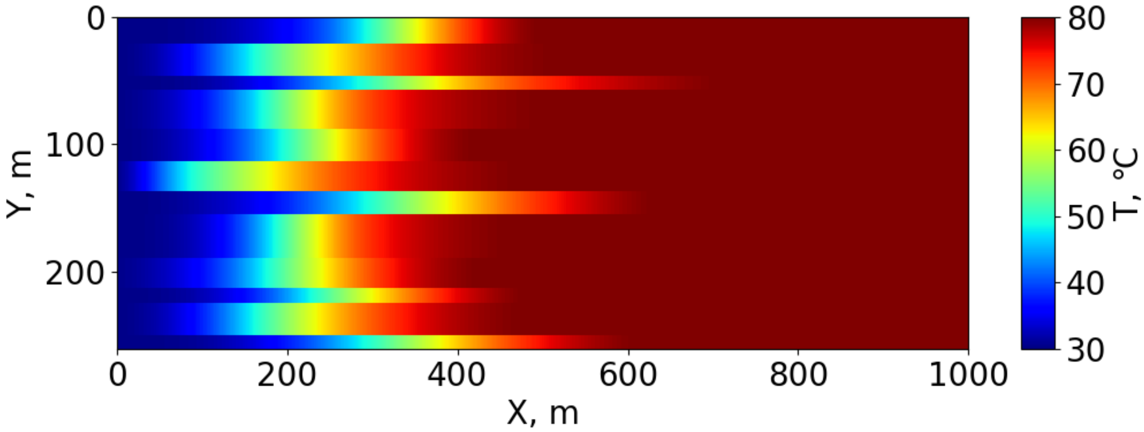

Figure 3. An example of Tang et al.'s upscaling technique with the original k_z with 12 layers after 10 years of production (Van Nieuwkerk, 2022)

Van Nieuwkerk also discovered that the upscaling results did not give a quantitative fit for the initial drop in the produced water temperature. This is problematic, considering how a geothermal doublet typically is shut down only shortly after the initial decline in temperature at the production well (Daniilidis et al., 2021). But when Van Nieuwkerk increased the vertical thermal conductivity parameter k_z, the production temperature predictions of the upscaled simulations improved significantly. Figure 4 shows how the fine-grid simulator's predictions in production temperature development are matched more accurately by Tang et al.'s new upscaling technique when k_z is doubled. In the figure, the upscaling method of Tang et al. with its normal thermal conductivity parameter is labelled 'Taylor' upscaling. The upscaled simulation with the increased thermal conductivity is labelled 'Taylor $k_z=2k_{zi}$' and the conventional upscaling technique is labelled 'Arithmetic'. To find out whether increasing the vertical thermal conductivity parameter is justified from a physical perspective, a simplified model of heat dissipation will be investigated in this thesis.

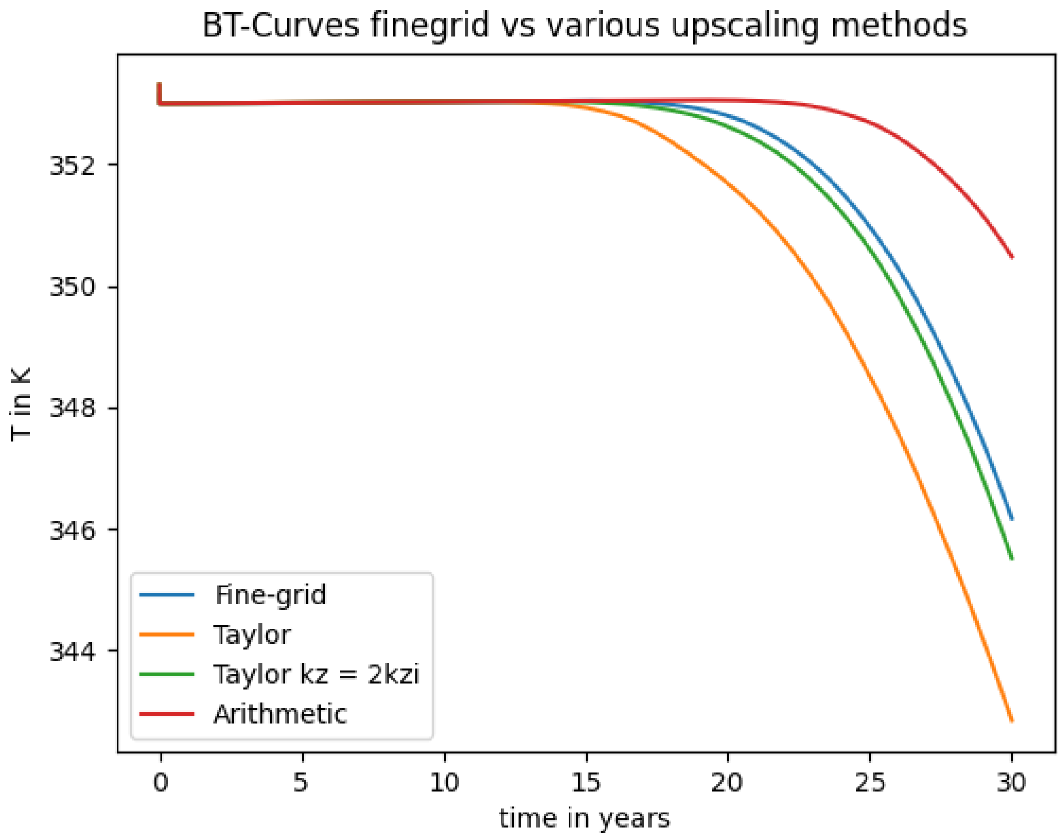

Figure 4. A plot that shows the drop in production temperature at the production well over time. Fine-grid results are compared to conventional arithmetic upscaling techniques, as well as Tang et al.'s Taylor upscaling techniques with the original $k_z = k_{zi}$ and $k_z = 2k_{zi}$ (Van Nieuwkerk, 2022).

2.5 Temperature distribution from Introductory Transport Phenomena

A layer-cake model will be considered in this thesis that imitates a fast-moving cold front through a geothermal reservoir. The model contains an infinite alternating set of hot and cold layers with identical properties and dimensions. In the model, conduction is assumed to be the only mechanism that transfers heat from the hot to the cold layers. This model is analogous to solutions from existing literature. In Example 11.5-2 found in *Introductory Transport Phenomena* by Bird et al. (2013), the authors derive a solution for temperature decay over time in a 'Finite Width Slab'. The finite width slab has constant physical properties and width '$2b$'. At $t \leq 0$, the temperature is constant at $T = T_0$ all throughout the slab. Then at $t = 0$, both the top and the bottom of the slab are suddenly heated and maintained at a fixed temperature $T = T_1$ for all $t > 0$.

Bird et al. have plotted the solution that arises from the infinite Fourier series that provides the temperature profile throughout the slab. The results can be seen in Figure 5. The authors made the solution as applicable as possible by translating the equation into dimensionless form. In the figure, $^{\mathrm{y}}/_{\mathrm{b}}$ indicates the dimensionless position coordinate in the slab. The temperature at $^{\mathrm{y}}/_{\mathrm{b}} = 0$ represents the temperature in the centre of the slab. But, although the thickness of the slab is '$2b$', the figure only shows a maximum dimensionless position of $^{\mathrm{y}}/_{\mathrm{b}} = 1$. The reason for this is that the finite width slab that the authors solve for has a symmetrical temperature distribution, which means that only half the cross-sectional area of the slab is required to still know the temperature at any position.

To transfer temperature into dimensionless form, $\theta = \frac{T_1 - T}{T_1 - T_0}$ and $\theta^* = \frac{T - T_0}{T_1 - T_0}$ are used on the y-axes. The authors display the temperature distribution as a function of time by including the dimensionless time variable $\tau = \frac{\alpha t}{b^2}$. Here, b is the half of the thickness of the plate and t the time since initial heating. α represents the thermal diffusivity parameter $\alpha = \frac{k}{\rho C_p}$ with k being the thermal conductivity parameter, ρ the density and C_p the heat capacity of the slab. With a higher value for $\tau = \frac{\alpha t}{b^2}$, temperature will be more evenly distributed throughout the slab.

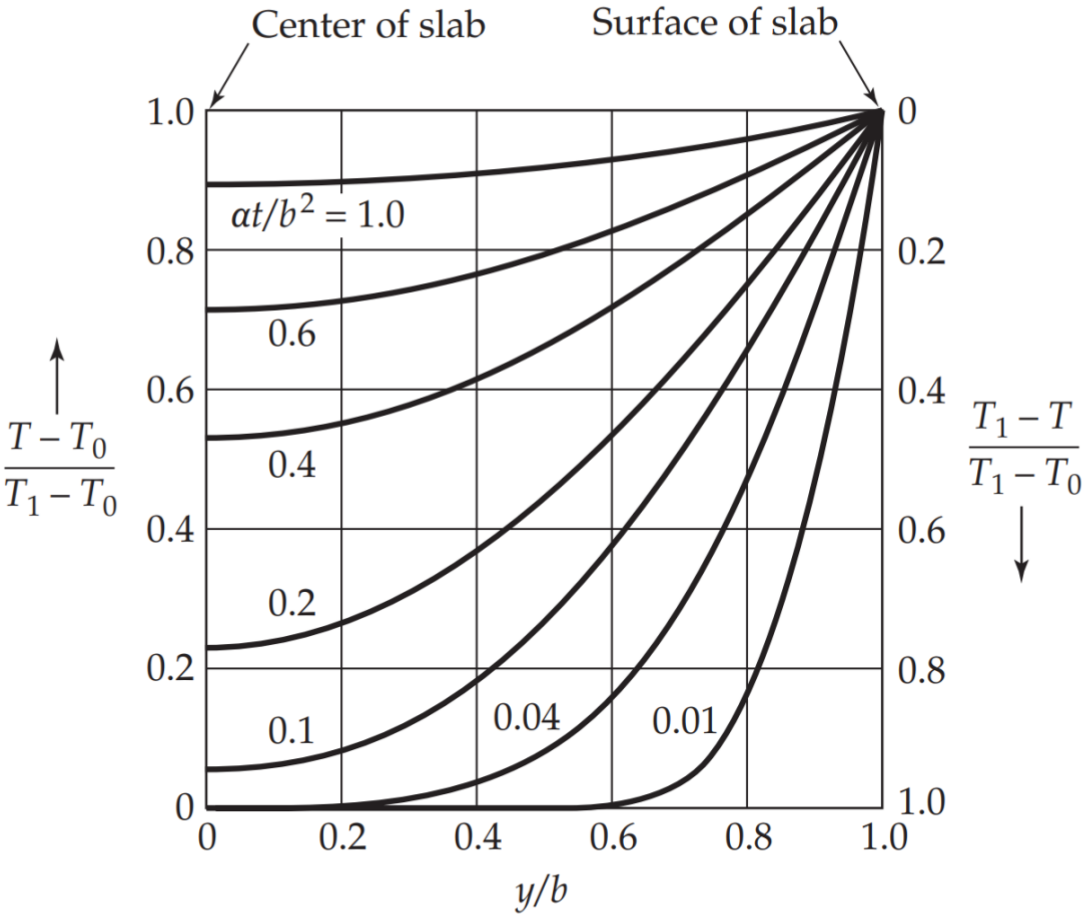

Figure 5. Temperature profiles for unsteady-state conduction in a slab of finite thickness 2b (Bird et al., 1987)

The mathematical function used to make this graph starts with a shell balance on an element of differential width. The authors then obtain the following infinite series for dimensionless temperature as a function of time and position:

$$\frac{T_1 - T(y,t)}{T_1 - T_0} = 2\sum_{n=0}^{\infty} \frac{(-1)^n}{\left(n + \frac{1}{2}\right)\pi} * \exp\left[-\frac{\left(n + \frac{1}{2}\right)^2 \pi^2 \alpha t}{b^2}\right] * \cos(n + \frac{1}{2})\frac{\pi y}{b} \qquad (1)$$

2.6 Thermal decay from *Transport Phenomena Data Companion*

Another publication that displays the temperature loss over time for the same problem is shown in Section 2.5 can be found in the book *Transport Phenomena Data Companion* by Janssen & Warmoeskerken (1987). The solutions that are provided in this book solve for the temperature decay over time for a ‘plate.’ The plate that the authors refer to is identical to the ‘finite width slab’ as solved for by Bird et al. (2013).

Similar to the solutions provided by Bird et al., dimensionless variables are used. Figure 3 shows a plot of the average temperature throughout the slab decaying over time. The dimensionless time variable that Janssen & Warmoeskerken use is $< M > = \frac{T_1 - <T>}{T_1 - T_0}$, where $< T >$ represents the average temperature over the entire volume of the slab. Secondly, a plot of the centre temperature of the plate decaying over time is shown in Figure 6. Here, the dimensionless temperature that is used is $M = \frac{T_1 - T_c}{T_1 - T_0}$, where T_c represents the centre temperature of the slab. For the dimensionless time scale, the authors use $Fo = \frac{\alpha t}{d^2}$, where α represents the diffusivity parameter, t the time since initial heating and d the entire thickness of the plate.

Although the ‘plate’ from *Transport Phenomena Data Companion* is identical to the ‘finite width slab’ from *Introductory Transport Phenomena*, there is one difference. Instead of using a thickness of ‘$2b$’ as was done for the finite width slab, Janssen & Warmoeskerken define the problem as a plate of thickness ‘d’ that is heated from both sides, meaning that for the same problem $\mathrm{d} = 2 * \mathrm{b}$. However, since the tabulated plate solutions from Figures 6 and 7 uses the time scale $Fo = \frac{\alpha t}{d^2}$ in contrast to Bird et al.’s $\tau = \frac{\alpha t}{b^2}$. Because of this difference in dimensionless scales, the solutions of the slab cannot directly be compared to that of the plate. Because $d^2 = 4 * b^2$, the dimensionless time unit in the plate plot in Figures 6 and Figure 7 is moving four times quicker than that of the slab of Figure 2. Therefore, to fit results from Figure 5 in the same graph and adjust it to the Fo plate timescale, its slope will have to be four times as large.

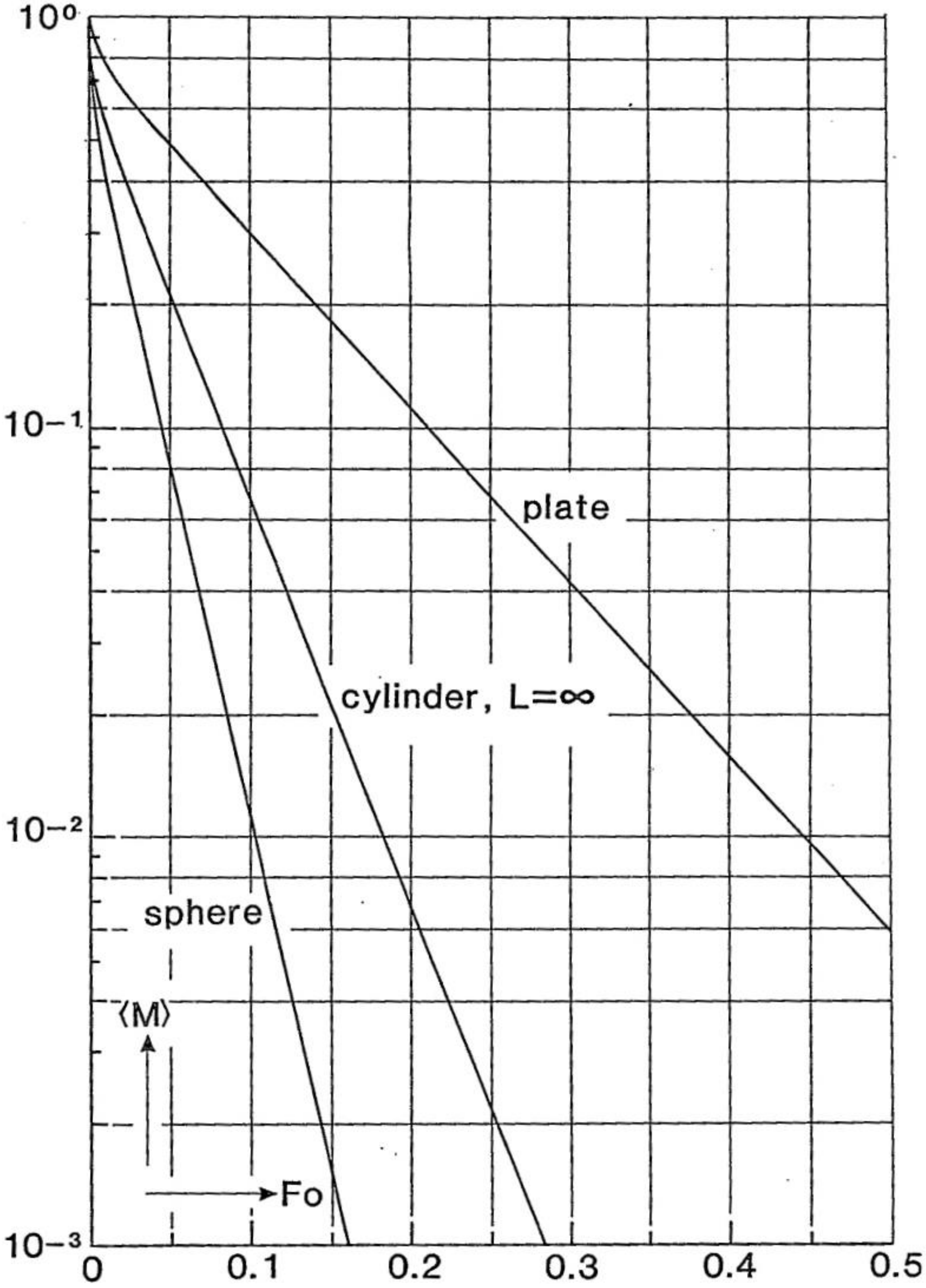

Figure 6. The average temperature of a plate that is heated on both sides plotted on a semi log scale (Janssen & Warmoeskerken, 1987)

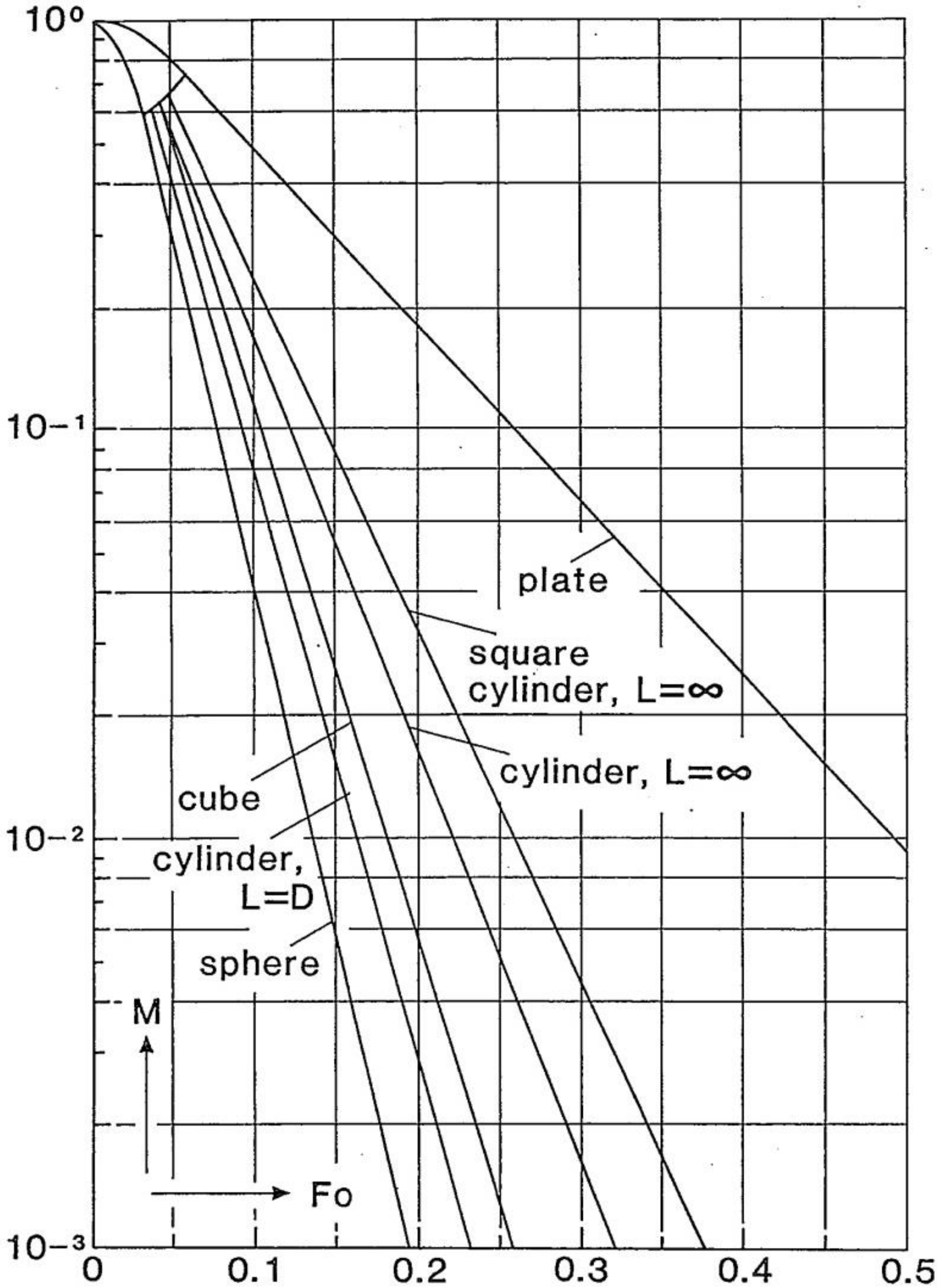

Figure 7. The centre temperature of a plate that is heated on both sides, plotted on a semi log scale (Janssen & Warmoeskerken, 1987)

3. Methodology

To investigate whether a valid physical reason exists for increasing the vertical hydraulic conductivity, four different cases will be considered. In Case 1, an energy balance will be derived for a model of a fast-moving cold front where the temperature at the boundary is suddenly raised to a new temperature in one step. From the energy balance, a dimensionless equation for temperature over time will be able to be derived by solving a first order ordinary differential equation. This equation will then be compared to existing analytical solutions in Case 2. In Case 3, the model from Case 1 will be used. However, in this scenario, the temperature at the boundary of the grid block will be raised in several steps to match reality more accurately using a technique from Transport Phenomena called ‘superposition’. With superposition, instead of applying just one temperature change, the total temperature change takes place more gradually in multiple steps. Then in Case 4, superposition will be applied on the analytical solutions to find the temperature over stepwise temperature increments. Finally, in the last section, a method will be proposed that can be used to provide a rough estimate of the rate of heating caused by the progression of the cold front.

3.1 Case 1: Finite difference modelling – one temperature change

This thesis utilises a layer-cake model to represent a fast-moving cold front in a geothermal doublet with warmer layers above and below is represented as an infinite series of alternating warm and cold layers with identical thicknesses and thermal properties. A schematic representation of a section of these alternating hot and cold layers is shown in Figure 8. Each layer in the model is assumed to always be at a uniform temperature. Initially, the cold layers are at uniform temperature T_0 and the hot ones are at uniform temperature T_2. Each layer has a thickness $2H$, length L, width W. The cold layers represent the high permeability zones in the reservoir where the rock has cooled down. The reservoir rock used in this model has thermal conductivity k, density ρ and heat capacity C_p.

This model will only consider heat conduction as a mechanism of heat transfer, meaning that possible effects of convection and heat generation will be neglected. Simplifying the model in this way allows us to compare the temperature of the layers directly to analytical solutions. Case 1 considers a single temperature increment, where the block is initially at T_0 and then suddenly brought into contact with the hot layer, thereby heating up at the boundary to the new temperature, which will be the exact average of T_0 and T_2. In this case, an energy balance will be applied to half the original layer. This equation will be translated into dimensionless form to allow for simple comparison with the analytical solutions. Each layer in the model of Figure 5 resembles a ‘finite width slab’ of Section 2.5 and the ‘plate’ of Section 2.6.

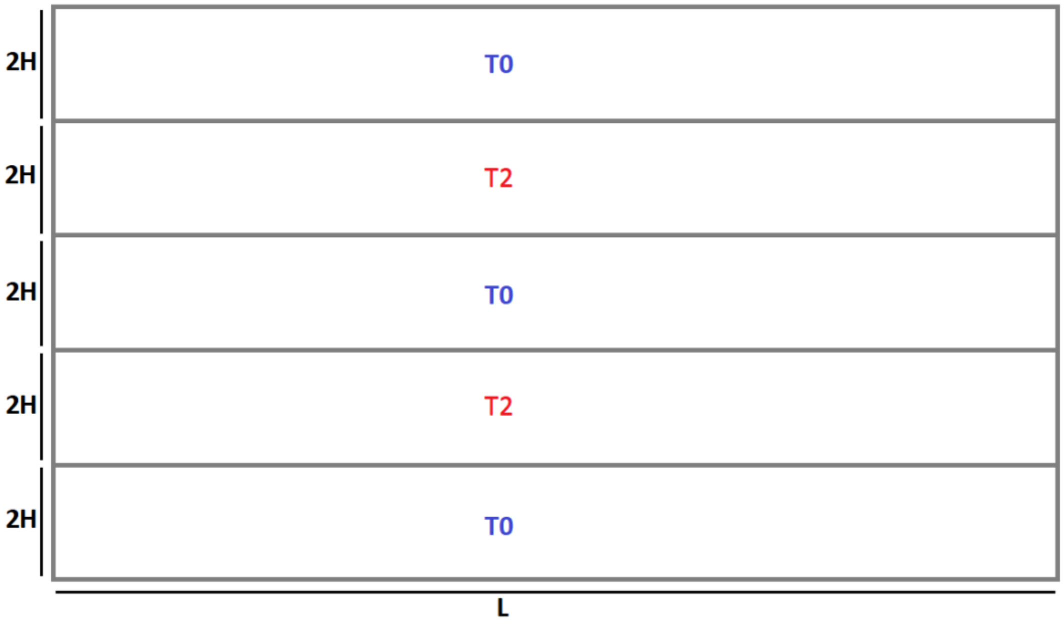

Figure 8. A section of an infinite series of two geological layers with identical dimensions and thermal properties, but with different uniform starting temperature

3.1.1 Recognizing symmetry

As can be seen in Figure 8, all layers are symmetric about their middle planes. At the middle of each layer, the same amount of heat is flowing from the top down as from the bottom up. This means that no heat will flow through the middle of each layer. Physically, a no heat flow boundary can be treated identically to a perfectly insulated boundary (Ohio University, 2015). Furthermore, because the model is symmetric, all boundaries between layers will immediately jump to the average of the two initial temperatures; $T_1 = \frac{T_0+T_2}{2}$ **.** Eventually, when conduction continues as time goes on, the entire layer package will approach the same temperature T_1.

Because of the symmetrical nature of this model, each layer can be subdivided into two grid blocks with half the original thickness. Then, the block of half the original layer will have thickness H, length L and width W. A schematic representation of such a grid block is shown in Figure 9. Compared to the analytical solution from *Introductory Transport Phenomena* presented in Section 2.5, Figure 5's 'centre of slab' at position ${}^{\mathrm{y}}/_{\mathrm{b}} = 0$ would be analogous to the temperature at the fully insulated top in Figure

9. However, whereas Bird et al. calculate the finite width slab with variations in temperature within the grid block, the model as shown in Figure 6 treats the block as steady state.

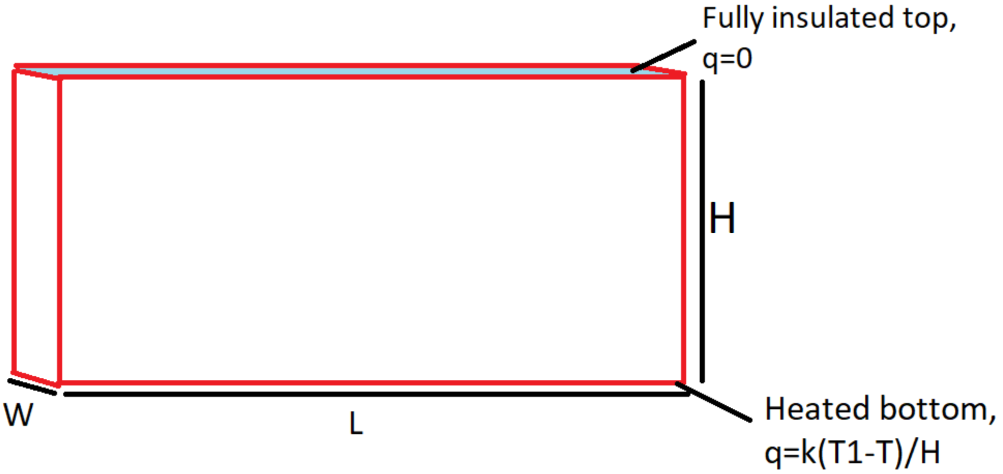

Figure 9. A schematic representation of the steady-state grid block model

3.1.2 Defining the system

Since the middle of each layer from Figure 8 is a zone boundary of no heat flow, each of the grid blocks has a boundary that can be treated as fully insulated. The other boundary of each half is a grid block boundary. The temperature at the boundary is known to be $T_1 = \frac{T_0+T_2}{2}$. At time $t = 0$, the bottom surface of the block is instantly changed to temperature $T = T1$, and heat is conducted into the bottom surface of the block according to Fourier's law. Through Fourier's law of thermal conduction, heat flux q_z coming in from the grid block boundaries can be calculated with the following equation (University of Ottowa, 2007):

$$q_{z,conduction} = \frac{k(T_1 - T)}{H} \tag{2}$$

In this equation, H is the thickness of the grid block half, T is the temperature, and k represents the thermal conductivity parameter.

3.1.3 Applying an energy balance to the grid block

The general form of the energy balance is as follows:

$$\begin{gathered}[\text{Transport of thermal energy into system}]\\ -\\ [\text{Transport of thermal energy out of system}]\\ +\\ [\text{Amount of net release of thermal energy generated in the system}]\\ =\\ [\text{Amount of thermal energy accumulated in the system}]\end{gathered}$$

Heat flows from high temperature to low temperature. This means that in the grid block model of Figure 6, thermal energy will flow from the heated bottom towards the top surface. Because the top surface of the grid block is treated as fully insulated, there will be no transport of thermal energy out of this system. Furthermore, since this model neglects generation of thermal energy within the grid block, the third thermal energy generation term drops out of the equation. Then, as only conduction is taken into account in this model, the energy balance used in Case 1 can be reduced to the following:

$$\begin{gathered}\text{[Conduction into the system]}\\ =\\ \text{[Amount of thermal energy accumulated in the system]}\end{gathered}$$

3.1.4 The equations for the energy balance

Conduction into the system can be approximated by multiplying heat flux q with the surface area A that the flux is applied on:

$$Q = A * q_{z,conduction} \tag{33}$$

In this equation, Q represents the total amount of heat energy conducted into the block. After having substituted in the equation for the surface area of the bottom $A = length * width$, along with Eq. 2, Eq. 3 becomes:

$$Q = L * W * \frac{k * (T_1 - T)}{H} \tag{44}$$

Accumulation of heat in the system can be approximated with the heat storage equation (Wu, 2010), as follows:

$$Q = V * \rho * C_p * \frac{\delta T}{\delta t} \tag{55}$$

In (5), Q represents the thermal capacity of the block and V its volume. The combined density ρ for the grid block can be found by $\rho = \rho_{matrix} * (1 - \varphi) + \rho_{pore\ fluid} * \varphi$, and the combined heat capacity is obtained with the equation $C_p = C_{p,matrix} * (1 - \varphi) + C_{p,pore\ fluid} * \varphi$. Here, φ indicates the total porosity of the grid block.

The last term of (5), $\frac{\delta T}{\delta t}$, shows the temperature change of the grid block over time. Next, after substitution of the volume $V = length * width * height,$ the equation of heat accumulation transforms into the following:

$$Q = L * W * H * \rho * C_p * \frac{\delta T}{\delta t} \tag{66}$$

3.1.5 Boundary conditions

Two boundary conditions are required to obtain an equation that can be used to derive the temperature of the grid block over time. The following boundary conditions will be used in the application of the energy balance:

1. The initial temperature at $t = 0$: $T = T_0$ at $t = 0$
2. The top surface is fully insulated: $q = 0\ at\ h = H$

3.2 Case 2: Analytical solutions

As the first significant decline of production temperature of geothermal doublets is most fundamental for their commercial use, this thesis focuses on the differences between the grid block model and the analytical solution in the first 40% temperature decline. In Case 2, a direct comparison will be made between the temperature development equation that has been derived in Case 1 and the analytical solution as displayed in Figure 3 of Section 2.6. From this comparison, the factor of increase of the thermal conductivity parameter will be calculated that will make the rate of change as predicted by the grid block model from Case 1 optimally fit the analytical solution for the first 40% of the total temperature loss. This process of calculating the factor of increase required of k_z will be repeated when comparing the superposition Cases 3 & 4 solutions. Additionally, in this section, a comparison will be made between the analytical centre temperature development that the two solutions from Sections 2.5 and 2.6 solve for. Here, the centre temperature results from Figure 5 of Section 2.5 will be plotted onto the centre temperature graph shown in Figure 7 of Section 2.6 to rule out the possibility of errors in the literature.

3.3 Case 3: Finite Difference Modelling – Five Temperature Changes

The grid block of Case 1 was ‘suddenly’ brought into contact with a hotter grid block at $t = 0$. However, this does not accurately resemble reality. As cold-front breakthrough in a geothermal well happens over the span of many years, the temperature difference between the cold and hot layers increases only slowly with continued thermal dispersion. Initially, the high permeability layers only have a slightly different temperature from its surrounding rock. However, as forced convection in the high permeability layers continues, thermal dispersion slowly becomes larger. Therefore, it would be more realistic to model Case 1 with several temperature increments. In Case 3, this is done through the application of the principle of ‘superposition’ from Transport Phenomena. When deriving an equation using superposition, the dimensionless time scale $\theta^* = \frac{T-T_0}{T_1-T_0}$ must be used (W.R. Rossen, personal communication, July 1, 2022). Translating $\theta = \frac{T_1-T}{T_1-T_0}$ to θ^* can be done easily, as $\theta^* = 1 - \theta$.

Using the equations derived in Case 3, the temperature at any interval between temperature increments can be obtained. Therefore, the temperature behaviour of the superposition solutions will be investigated for different dimensionless heating intervals $\tau_1 = \frac{\alpha t_1}{H^2}$. When the rate of heating is happening at speed, solutions of the superposition results will converge towards the results obtained from Case 1. On the other hand, when the rate of heating is taking place very slowly, each temperature increment will already have heated up the block evenly by the time the next temperature increment takes place. In this thesis, a variety of heating intervals will be calculated. Intervals between temperature increments that will be plotted for are $\tau_1 = 0.025,\ 0.05,\ 0.1,\ 0.2,\ 0.4,\ 0.8,\ 1.6,\ 3.2,\ 4.$

3.4 Case 4: Analytical Solution - Five Temperature Changes

The principle of superposition is also used in Case 4, but now applied to the analytical solutions. This is done as to find out whether a stepwise change in temperature will make the finite difference solution from Case 3 match the analytical solution more accurately. The same set of temperature increase intervals will be used as in Case 3 to best compare the two solutions. Results of both cases will be plotted with the use of *Microsoft Excel*. Both the average and the centre temperature will be displayed in these plots. Additionally, a separate graph will be included that shows the absolute difference between the analytical and the finite difference solutions. The values required for the application of superposition to the analytical solution will be derived from a digital enlargement of Figure 6 from Section 2.5. The advantage of using a digitalized version of Figure 6 is that reading errors can be reduced to a minimum. Centre temperatures will be derived from Figure 5.

3.4.1 Application of superposition on analytical solutions

Applying superposition on analytical solutions works by reading off the changes produced by temperature increments that have taken place at different points in time. For example, to determine the average analytical superposition simultaneously as the last heating step has been applied, temperature values will have to be read off at $\tau = 0,\ 1\tau_1,\ 2\tau_1,\ 3\tau_1,\ 4\tau_1$. Therefore, after five temperature increments, the five different temperatures need to be used to find the superposition temperature.

3.5 Comparing Solutions

In this section, the rate of heating will be estimated on the basis of a real-life case taken from the manuscript by Tang et al. (2022) a superposition graph for comparison between Cases 3 & 4 at this apparent real-life heating rate will also be included. The rate of heating will be estimated by tracking the time it takes for the temperature of the fast-moving cold front to decrease 20% of the difference between T_0 and T_1. If the real-life heating rate corresponds to superposition results where the finite difference solution is not far off from the analytical solution, this would mean there would be no apparent reason as to why increasing k_z would be valid. But, if the real-life rate of heating resembles a situation where the finite difference solution and the analytical solution are still very different, this indicates that there could be a valid physical reason as to why increasing k_z would be justified.

4 Results

In this chapter, the results of all four cases will be discussed. Finally, a heating rate estimate will be made in the last section on a fast-moving cold front from a simulation provided by P. van Nieuwkerk.

4.1 Case 1: Finite difference modelling – one temperature change

This section addresses the results obtained from the Case 1 model. Section 4.1.1 will provide the derivation of the equation that shows the temperature over time in the grid block model. Section 4.1.2 will then translate this equation into a dimensionless form. The manner in which the Case 1 results would need to be converted to make the modelled results directly comparable to analytical temperature development results from the existing literature, will ultimately be discussed in Section 4.1.3.

4.1.1 Deriving an equation for steady-state temperature of the grid block over time

For the purpose of finding an equation that shows the temperature of the geological layer over time, the energy balance can be turned into a simple differential equation that can be solved by hand mathematically. As has been discussed in the methodology, the energy balance of the grid block model used in Case 1 can be reduced to just two terms:

$$\begin{gathered}[\text{Conduction into the system}] \\ = \\ [\text{Amount of thermal energy accumulated in the system}]\end{gathered}$$

Equating the previously derived Eq. 4 for conduction into the system with the equation for thermal energy accumulation Eq. 7 gives:

$$L * W * \frac{k * (T_1 - T)}{H} = L * W * H * \rho * C_p * \frac{\delta T}{\delta t} \tag{7}$$

By dividing both sides by $-L * W * k * \delta T$, Eq. 7 turns into the following:

$$\frac{(T - T_1)}{\delta T} = -\frac{H^2 * \rho * C_p}{k * \delta t} \tag{8}$$

Eq. 8 can now be rewritten so that a differential equation is obtained that can be solved easily:

$$\frac{\delta T}{(T-T_1)} = -\frac{k * \delta t}{H^2 * \rho * C_p} \tag{9}$$

Then, integrate on both sides:

$$\int \frac{1}{(T-T_1)} \delta T = -\int \frac{k}{H^2 * \rho * C_p} \delta t \tag{10}$$

Solving this integral gives:

$$\ln(T-T_1) = -\frac{k * t}{H^2 * \rho * C_p} + C \tag{11}$$

Here, C represents the integration constant. Consequently, Eq. 11 is rewritten into:

$$(T-T_1) = \hat{C} e^{-(\frac{k*t}{H^2 * \rho * C_p})} \tag{12}$$

In Eq. 12, $\hat{C}$ is the integration constant. Simplifying this leads to the equation can be obtained for temperature as a function of time:

$$T = T_1 + \hat{C} e^{-(\frac{k*t}{H^2 * \rho * C_p})} \tag{13}$$

The thermal diffusivity parameter $\alpha = \frac{k}{\rho C_p}$ can be substituted to obtain a more simplified version of Eq. 13:

$$T = T_1 + \hat{C} e^{-(\frac{\alpha t}{H^2})} \tag{14}$$

The integration constant $\hat{C}$ can be found by using the boundary condition that states that $T = T_0$ at $t = 0$. The resulting final equation then becomes:

$$T = T_1 + (T_0 - T_1) e^{-(\frac{\alpha t}{H^2})} \tag{15}$$

4.1.2 Translation to dimensionless form

The final temperature Eq. 15 can be translated into dimensionless form with dimensionless time $\tau = \frac{\alpha t}{H^2}$ and dimensionless temperature $\theta = \frac{T_1 - T}{T_1 - T_0}$. Translated to dimensionless temperature, T_0 becomes $\theta_0 = \frac{T_1 - T_0}{T_1 - T_0} = 1$. T_1 translated to dimensionless temperature gives zero, as $\theta_1 = \frac{T_1 - T_1}{T_1 - T_0} = 0$. Thus, Eq. 15 translated to dimensionless form becomes:

$$\theta = e^{-\tau} \tag{16}$$

4.1.3 Analytical Solutions – One Temperature Change

As has been discussed in Section 2.5, the temperature values from Figure 5 must be multiplied by four to translate them to the scale used in Figure of section 2.6. This also applies to results from the model of Case 1, as Case 1's 'H'' translates directly to the 'b' from Bird et al.. Therefore, the temperature results from Case 1 Eq. 15 will need to be multiplied by four to be translated correctly onto the time scale used in Figure 6.

4.2 Case 2: Comparison with Case 1 solution

From the MSc thesis in preparation by P. van Nieuwkerk it has been found that increasing the thermal conductivity value k_z has led to more accurate modelling results. In this first section of the temperature distribution graph, the slope of the Case 1 solution is diverging the most from the analytical plate-solution. In the first 40% of heat loss, which this thesis is focused on, the analytical plate solution has an even steeper slope than in its later temperature development sections. Figure 10 shows the results of Eq. 16 plotted onto the analytical solution graph of Section 2.6 with a red line.

If one wanted to make the solution from Case 1 fit the plate solution from *Transport Phenomena Data Companion* better, an adjustment to the k_z parameter can be made. If, for instance, the k-exponent from Eq. 1 would be doubled, the Case 1 solution Eq. 15 exponent would increase accordingly. For the first 40% loss in temperature, the solution from Case 1 takes a dimensionless time $\mathrm{Fo} = 0.128$. Meanwhile, the analytical plate solution only takes up dimensionless time $Fo = 0.031$to have lost 40% of its heat. Therefore, to fit the plate solution, k_z should be adjusted to a value $0.128/0.031 = 4.1$ times as large as the original. The blue line in Figure 8 displays the Case 1 solution Eq. 15 with this increased k_z parameter.

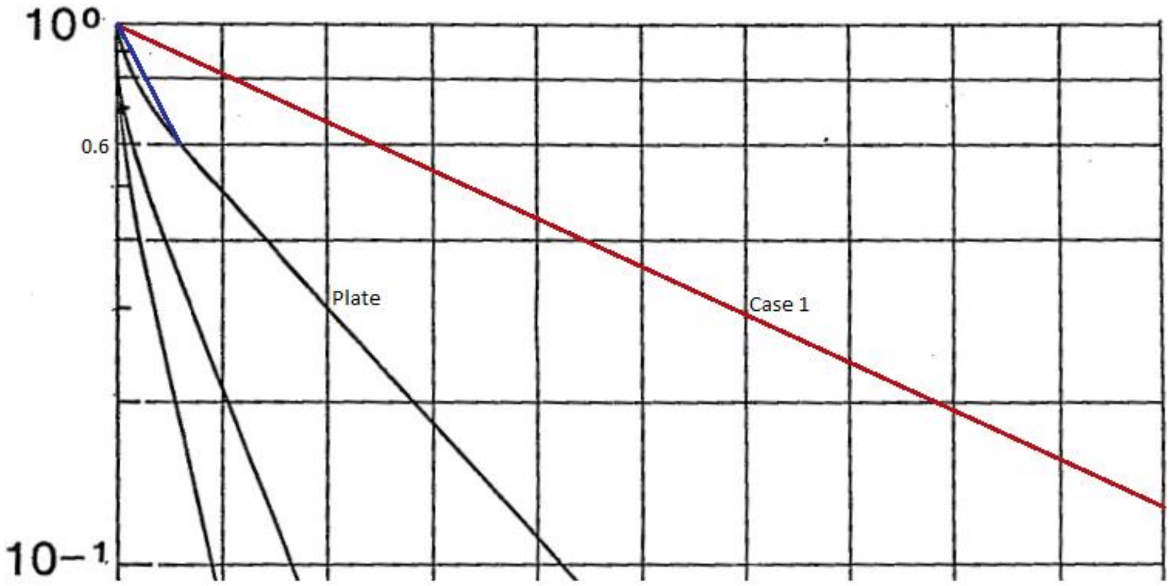

Figure 10. The finite-difference solution derived in Case 1 plotted with a red line onto the analytical plate solution from Section 2.6. The blue line shows how an increase in the thermal conductivity of Eq. 15 can produce a better fit (Adapted from: Janssen & Warmoeskerken, 1987).

4.2.1 Centre temperature comparison

Two different analytical solutions have been used in this thesis. Figure 11 displays how the two analytical solutions relate. Centre temperature results of Section Figure 5 from *Introductory Transport Phenomena* by Bird et al. have been plotted onto the centre temperature semi log plot of Section 2.6 Figure 4 from *Transport Phenomena Data Companion* by Janssen & Warmoeskerken. Both authors find the same temperature development for the same problem, as both solutions almost completely overlap. Therefore, the possibility of flaws in the analytical solutions highly unlikely.

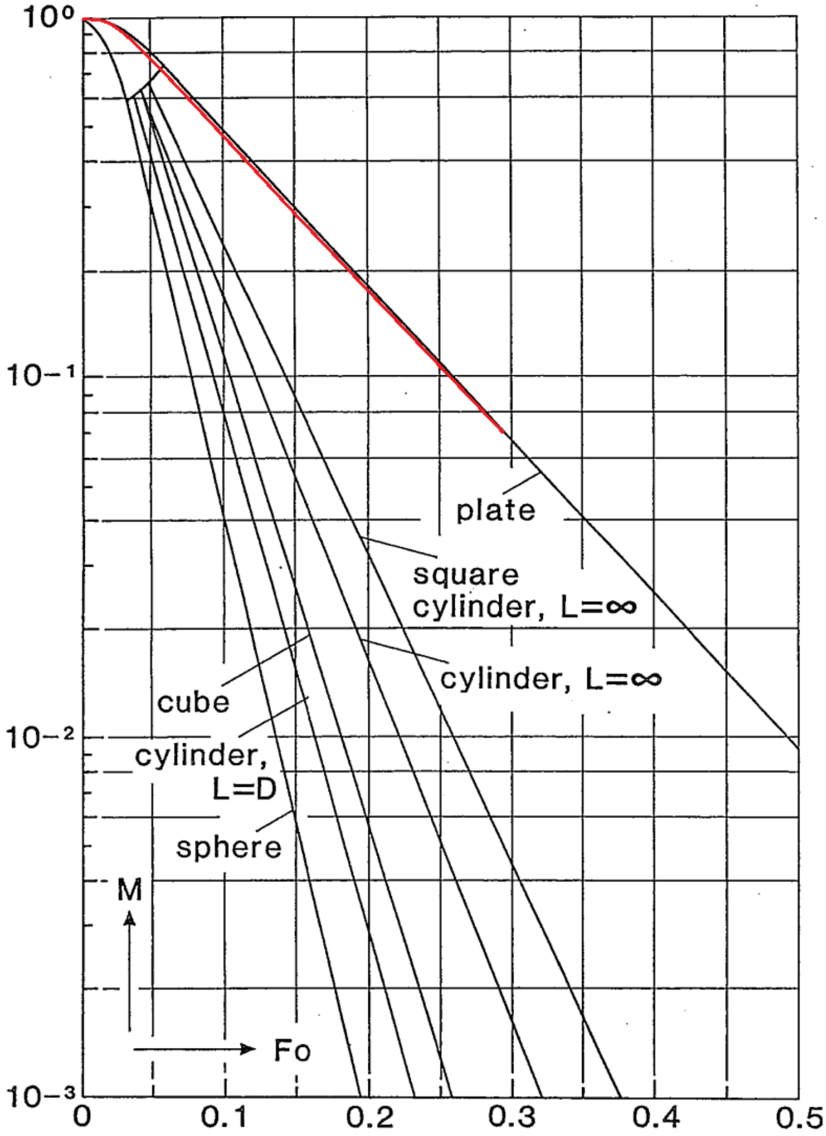

Figure 11. A comparison that displays the centre temperatures over time from Bird et al. mapped onto the centre temperature plot from Section 2.6. Both publications predict an almost identical temperature development (Adapted from Janssen & Warmoeskerken, 1987).

4.3 Case 3: Finite Difference Modelling – Five Temperature Changes

Instead of one sudden temperature increment at the bottom of the grid block from temperature T_0 to T_1, temperature in Case 3 is now raised in n steps at an interval τ_1. Since the final temperature difference that will be reached is $(T_1 - T_0)$, this means that each step will raise the temperature at the bottom surface by $\frac{1}{n} * (T_1 - T_0)$. To adapt the model from Case 1 to a situation with multiple heating steps, the principle of superposition can be used. Superposition can only be used with dimensionless form $\theta^* = \frac{T-T_0}{T_1-T_0}$. Translating Eq. 16 into θ^* gives the following equation:

$$\theta^* = 1 - e^{-\tau} \tag{17}$$

In this application of superposition, the entire stepwise heating process is taking place in $n = 5$ steps. Consequently, starting at $\tau = 0$, temperature is raised with $\frac{1}{5}$ or 20% of the temperature difference $(T_1 - T_0)$. Then, at $\tau = \tau_1$, the temperature is raised with another 20% and becomes 40% $(T_1 - T_0)$. At the third temperature increase at $\tau = 2\tau_1$, temperature at the bottom surface will be raised from the initial temperature with 60% of $(T_1 - T_0)$. At $\tau = 3\tau_1$, temperature at the bottom surface will be heated with 80% of the temperature difference $(T_1 - T_0)$. Finally, temperature at the bottom surface will be raised and maintained at 100% T_1 at $\tau = 4\tau_1$. The temperature at the bottom of the grid block is shown in Figure 12 below.

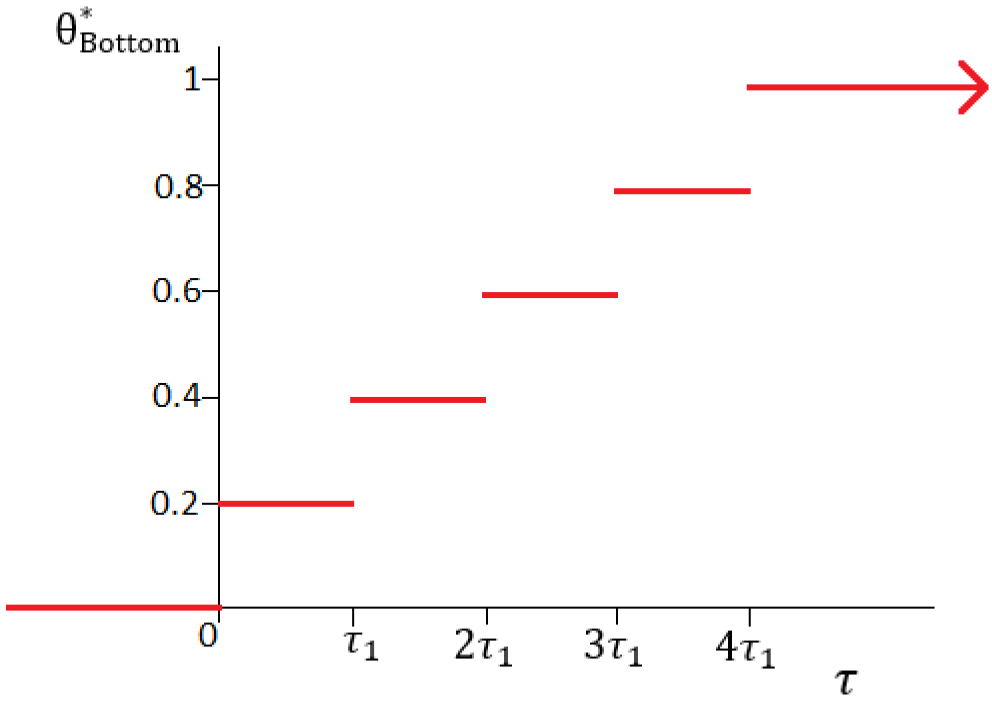

Figure 12. Temperature at the heated bottom of the model shown in Figure 3 increasing in $n = 5$ steps

4.3.1 Superposition at each time stamp

The effect of each heating step can be found through adapting Eq. 17 with time convolution. For instance, when the second temperature increment is initiated at $\tau = \tau_1$, the first temperature increment will already have had its effect during the entirety of τ_1. At any point in time, the resulting temperature θ^* can be calculated with the summation $\theta^* = \frac{1}{n}\sum \theta_i^*$ that contains the effect of each temperature increment that has set in at that time. The effect of each temperature increment at different time steps can be calculated with the following adaptation of Eq. 17:

$$\theta_i^* = 1 - e^{-\tau_i}$$

$$\text{With } \tau_i = \tau - (i-1)\tau_1 \qquad (18)$$

$$\text{And } i = \{1, \dots, n\}$$

Then, the temperature can be calculated for each interval with the following equations:

$$\theta^* = 0.2 * (1 - e^{-\tau}) \qquad (19)$$
$$\text{For } 0 > \tau > \tau_1$$

$$\theta^* = 0.2 * ((1 - e^{-\tau}) + 0.2 * \left(1 - e^{-(\tau - \tau_1)}\right)) \qquad (20)$$
$$\text{For } \tau_1 > \tau > 2\tau_1$$

$$\theta^* = 0.2 * (1 - e^{-\tau}) + 0.2 * \left(1 - e^{-(\tau - \tau_1)}\right) + 0.2 * \left(1 - e^{-(\tau - 2\tau_1)}\right) \qquad (21)$$

For $2\tau_1 > \tau > 3\tau_1$

$$\theta^* = 0.2 * (1 - e^{-\tau}) + 0.2 * \left(1 - e^{-(\tau-\tau_1)}\right) + 0.2 * \left(1 - e^{-(\tau-2\tau_1)}\right) + 0.2 * \left(1 - e^{-(\tau-3\tau_1)}\right) \tag{22}$$

For $3\tau_1 > \tau > 4\tau_1$

$$\theta^* = 0.2 * (1 - e^{-\tau}) + 0.2 * \left(1 - e^{-(\tau-\tau_1)}\right) + 0.2 * \left(1 - e^{-(\tau-2\tau_1)}\right) + 0.2 * \left(1 - e^{-(\tau-3\tau_1)}\right) + 0.2 * \left(1 - e^{-(\tau-4\tau_1)}\right) \tag{23}$$

For $\tau > 4\tau_1$

4.4 Case 4: Analytical Solution - Five Temperature Changes

The application of superposition to the analytical solutions works according to the same principle as has been used in Case 3. To find the resulting superposition temperature $\theta^* = \frac{1}{n}\sum \theta_i^*$ can again been used. Only this time, the temperature effects of the different temperature increments θ_i^* have been found through reading off the values from the analytical solution of Figure 5 from *Transport Phenomena Data Companion*. Again, the interval between heating intervals τ_1 has been changed to compare analytical and finite-difference superposition behaviour. Superposition temperature results for both the analytical as the grid block Case 3 solution are discussed in the section below for $\tau_1 = 0.025, 0.05, 0.1, 0.2, 0.4, 0.8, 1.6, 3.2, 4$.

4.4.1 Superposition results

The results from having applied superposition to both the grid block solution and the analytical solutions are shown in Appendices 1 & 2. The temperature values that have been derived from Figure 5 are shown in separate tables in Appendix 1. Each table represents a different heating rate. Appendix 2 displays the semi log plots that result from Cases 3 & 4 for all superposition heating intervals. The semi log plots from Appendix 2 show a clear trend: the bigger the heating interval, the more the temperature predictions of the two different solutions converge.

For smaller τ_1 values, the last temperature increment happens really soon after the first. The consequence of this is that the average temperature has only decreased by less than 10% of the final temperature difference when the last heating step is applied. Therefore, these graphs have been extended to the point where at least half of the final temperature difference has been reached.

Compared to the Case 1 & 2 solutions, the superposition grid block results do a much better job at matching the analytical solutions. Consequently, the factor of increase in k_z that produces an optimal fit in the first 40% temperature decrease now is much lower than the factor of 4.1 found from the comparison of Cases 1 & 2 in Section 4.2. At the time interval $\tau_1 = 0.1$, time interval, the best fit of the grid block solution to the analytical superposition solution can be found by increasing k_z by a factor of 2.5. At a heating interval $\tau_1 = 0.8$, the incongruence between solutions has decreased significantly. Now, the factor of increase required of k_z to produce an optimal fit has been reduced to a factor of 1.4. When the time interval between heating steps becomes longer, the factor of increase required of k_z becomes even lower. When the rate of heating is stretched to $\tau_1 = 4$, the two different solutions become virtually indistinguishable.

The reason for the two different solutions converging when the heating rate is lowered significantly is as follows. When the heating rate is exceptionally low, the interval between heating steps will be stretched out over time. As a consequence of stretching the heating steps out over a very long interval, the effect of the previous heating step will have already set in completely when the new heating increment is applied. Physically, this means that the previous heating step has now already distributed its temperature everywhere throughout the grid block. Considering that even if the analytical solution and the grid block solution are a factor of magnitude off from each other, they will then both predict that with long enough time, the temperature reached in the grid block will reach an equilibrium temperature that is equal to the bottom heating temperature. Consequently, when the time between heating steps becomes maximally large, both solutions will predict indistinguishable temperatures.

4.5 Estimating realistic heating rates

Figure 13 below shows a 12 layered simulation of a geothermal reservoir after 20 years of production. From this simulation, the heating rates of the two fast-moving cold temperature fronts, marked by the two white arrows, will be investigated. Although the top and the bottom layers of this simulation also appear to be a fast-moving cold front, their lower temperatures are controlled by the under- and overburden. As the influence of the under- and overburden is not taken into consideration in the model used in this thesis, these layers will not be used to estimate the heating rates.

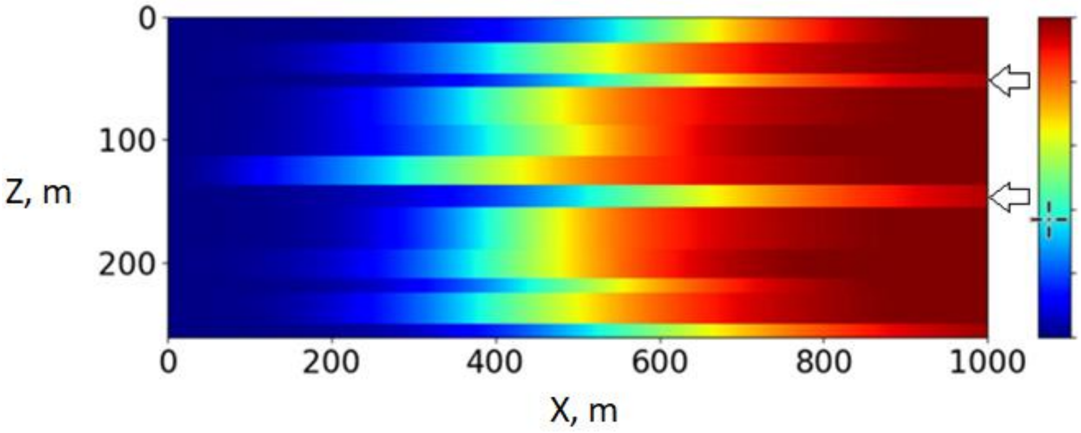

Figure 13. A simulation based on Tang et al.'s upscaling technique with the original k_z with 12 layers, after 20 years of production (Van Nieuwkerk, 2022)

In Cases 3 & 4, the grid block was heated in five steps that each raised the temperature with 20% of the difference between initial and final temperatures. Therefore, estimates of a realistic heating rate can be made by finding the time it would take for the fast-moving cold front to have cooled down by 20% of the difference between the initial and final temperatures. In Cases 3 & 4, one heating interval $\tau_1 = \frac{\alpha t_1}{H^2}$ represents 20% temperature difference. Therefore, to estimate the heating interval τ_1 from a reservoir simulation, the layer thickness H and the thermal diffusivity parameter α are needed, as well as t_1 . The time t_1 signifies the amount of time it takes for the fast-moving cold front to have heated up by 20%. From the simulation, the thermal diffusivity parameter α is known to be $\alpha = 1.15 * 10^{-6}\ {}^{m}/_{s}$. The layer thicknesses H of the top fast-moving front is 10 meters, and that of the bottom one is 18 meters.

To find the time t_1, the time it takes the cold front to heat up by 20% is needed. In Figure 13, both fast-moving layers have a temperature of approximately 65°C at $X = 750m$. At $X = 900m$, both fast moving-layers have a temperature of approximately 75 °C. This means that the fast-moving front takes up 150 meters to heat up by 20% of the temperature difference between the initial and final reservoir temperatures. Then, assuming that thermal dispersion of each layer takes place at a constant rate, the velocity of the layer can be estimated by dividing the distance that the fast-moving section has moved from the origin by the total amount of time it took to move from the origin. The distance that is used to estimate the velocity of this section is taken at $X = \frac{750+900}{2} = 825m$, as this marks the distance from the origin to the middle of the section. Since the time that it took for this fast-moving section to travel there is 20 years, velocity is estimated at $v = \frac{x}{t} = \frac{825\ m}{20\ years} \approx 41\ {}^{m}/_{year}$. This means that as the fast-moving front heats up 20% in 150 meters, $t_1 = \frac{x}{v} = \frac{150}{41} \approx 3.7$ years, or $t_1 \approx 1.17 * 10^8$ seconds. Therefore, τ_1 estimates for both of the fast-moving cases are the following:

$$\tau_{1,top\ layer} = \frac{\alpha t_1}{H^2} \approx \frac{1.15 * 10^{-6} * 1.7 * 10^8}{10^2} \approx 1.35$$

and

$$\tau_{1,bottom\ layer} = \frac{\alpha t_1}{H^2} \approx \frac{1.15 * 10^{-6} * 1.17 * 10^8}{18^2} \approx 0.4$$

4.6 Finding the optimal fit

Figures 14 and 15 display the Cases 3 & 4 solution with the rough estimates of two heating rates, found as described in the previous section. The plots in the first 40% of temperature drop-off of the analytical results contain additional data points compared to the other plots from Appendix 2 in order to include more detail. This has been done to increase the validity of the analytical superposition results, as more data points in the first section of temperature drop-off will ensure that the non-linear temperature behaviour of the analytical solutions from Figures 6 and 7 is incorporated.

The figures show how the highest rate of temperature change takes place immediately after each heating step has been applied. This can be explained using the initial high rates of temperature change. Since the centre temperature plot from Figure 7 shows a slope that goes down more gently at the initial decrease in temperature, the average temperature plot shows a steeper initial decline than the centre temperature plot does. At the higher heating rate of Figure 15, both the analytical centre temperature and average temperature show almost identical development over time. The reason for this is that at longer spans of dimensionless time, the end temperature of each heating step has nearly been reached already when the next heating step starts.

For the $\tau_1 = 0.4$ scenario, the factor of increase for k_z that would be required to optimally fit the steady-state grid block solution to the first 40% temperature drop-off of the analytical solution would be 1.79. For $\tau_1 = 1.35$, this factor of increase for k_z would only be 1.18. In either case, the required factor of increase in the thermal conductivity remains much lower than the original factor of 4.1 from Cases 1 & 2.

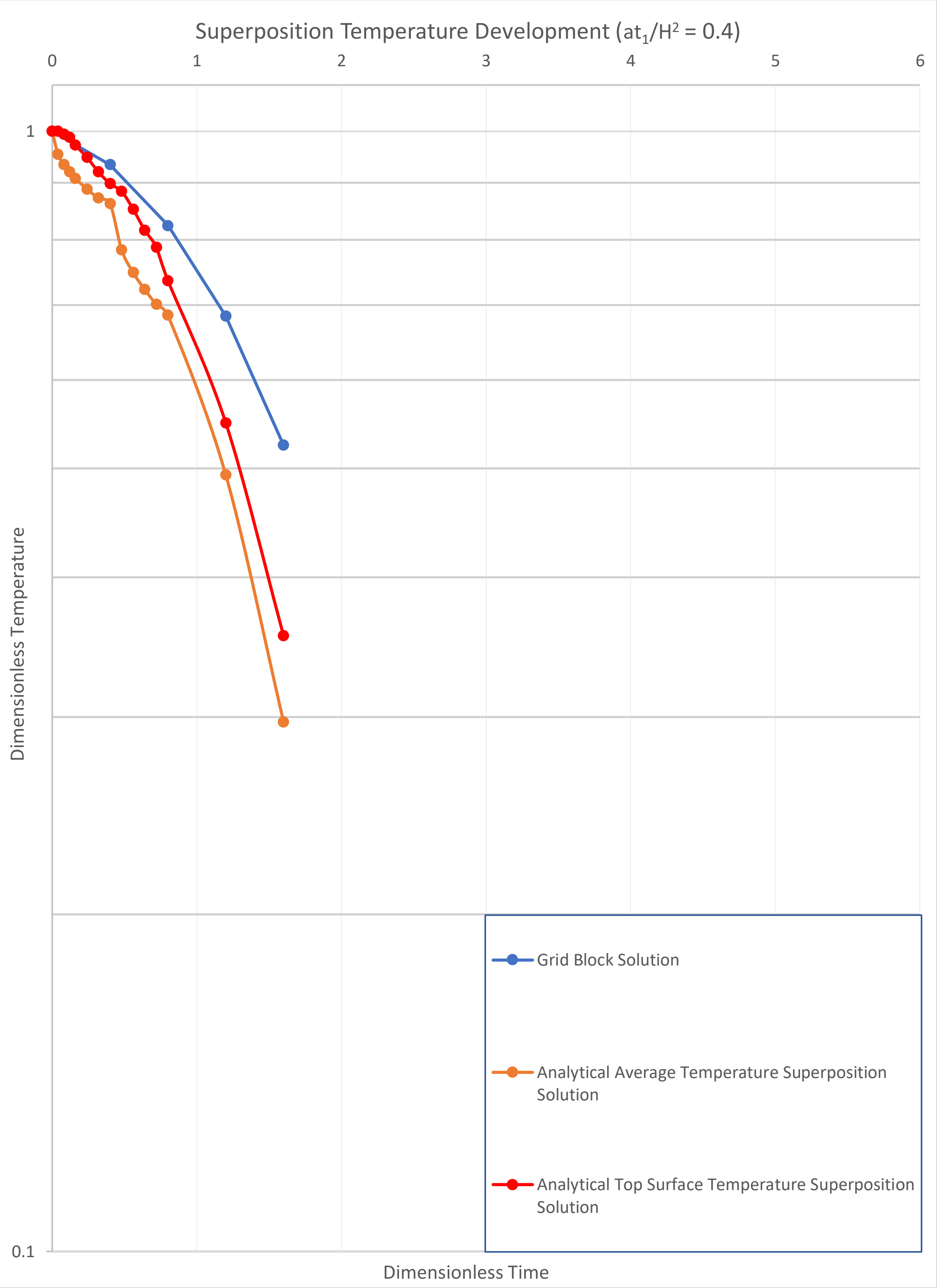

Figure 15. A plot that compares modelled superposition results with temperature increments at a heating interval of $\tau_1 = \frac{\alpha t_1}{b^2} = 0.4$ *against the analytical superposition solution from Transport Phenomena Data Companion*

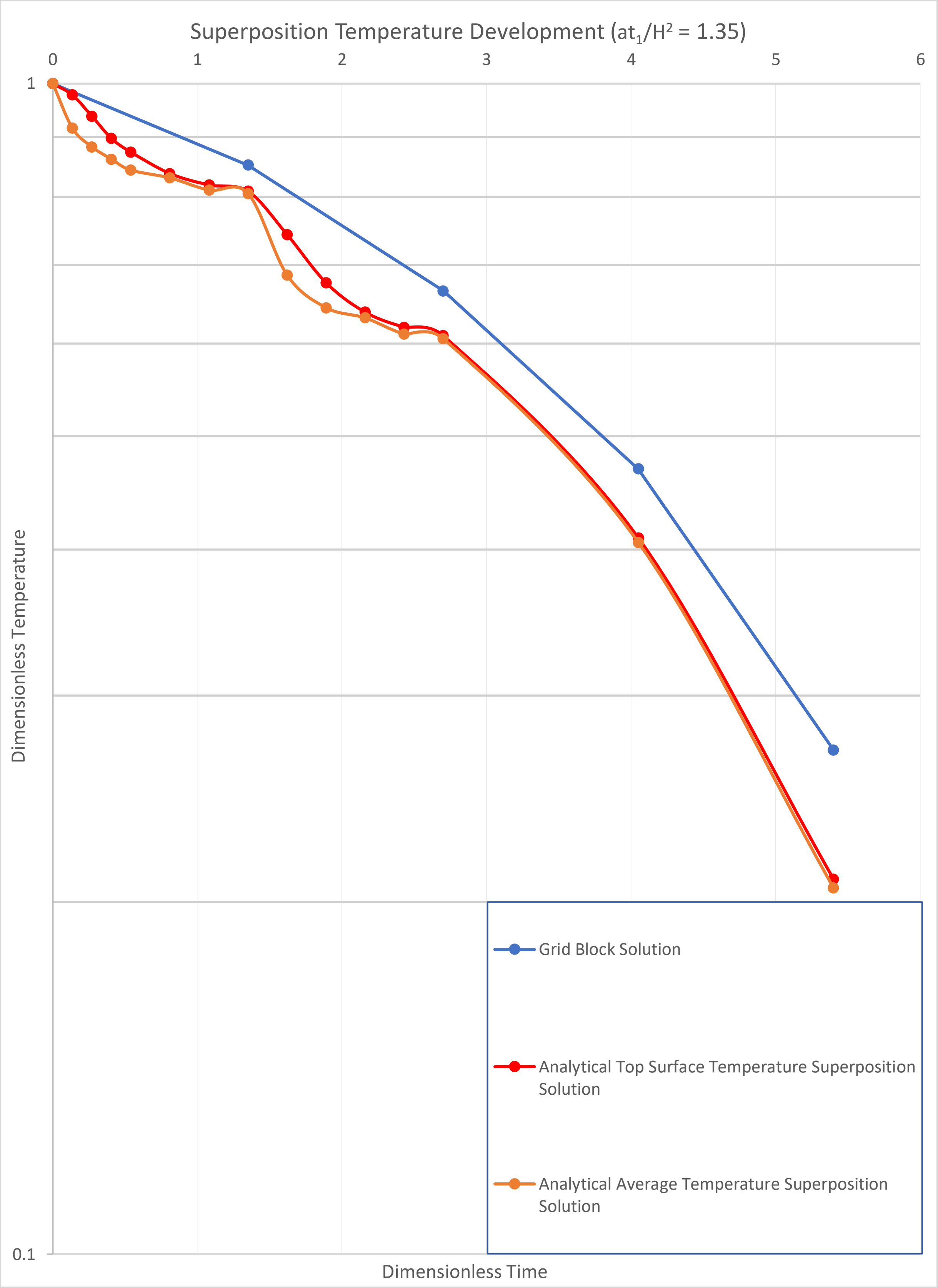

Figure 14. A plot that compares modelled superposition results with temperature increments at a heating interval of $\tau_1 = \frac{\alpha t_1}{b^2} = 1.35$ *against the analytical superposition solution from Transport Phenomena Data Companion*

5. Research Limitations

Several of the results obtained from this thesis remain to be investigated in more detail. For this thesis, a simplified model of fast-moving cold fronts was considered. This was done deliberately, as analytical solutions for such a problem already exist. In the model, only conduction was considered as a mechanism of heat transfer. This means that effects caused by convection were left out when determining the results.

The model of a fast-moving cold front was derived from a situation that was made up of an infinite series of alternating high and low temperature layers with identical constant properties and thicknesses. However, such a model is by no means fully representative of the physical situation as found in the actual subsurface. Reservoirs are often heterogeneous and do not have constant thermal properties. Simulations that were run by P. van Nieuwkerk show that the small amount of fast-moving cold temperature layers in a geothermal doublet simulation are oftentimes surrounded by a much thicker section of hot layers. Consequently, the hot reservoir rock that surrounds a fast-moving cold layer does in actuality show any significant signs of cooldown. This is in large contrast to what the model of infinite alternating layers of equal thickness shows. In this model, the hot layers cool down by the same amount that the cold layers heat up with.

Another shortcoming of this investigation is the fact that for establishing the analytical solutions in Case 4, a relatively low-resolution plot of temperature decay was used, which potentially resulted in reading errors. To counter this in future research, it is recommended to use the computer simulations of Eq. 1 from *Introductory Transport Phenomena* by Bird et al. (2013) to find the average temperature over time more precisely. In addition to this, the accuracy of the Case 4 result plots could be improved by adding additional data points to the analytical superposition solutions.

Furthermore, in Section 4.5, the heating rates of the fast-moving layers were estimated on the basis of one example of a geothermal doublet thermal dispersion simulation. The results of this specific simulation possibly do not represent a typical heating rate of fast-moving layers in geothermal wells. If results are invalid, it could also be the consequence of reading errors from Figure 13. Adding onto that, in the estimation of the heating rate, it was assumed that the fast-moving cold temperature layers move at a constant velocity over a span of several years, despite it being unknown whether this is the case.

6. Conclusions

Models of thermal dispersion in geothermal doublets that employ upscaling techniques have been found to give a poor quantitative fit for the first significant drop in produced water temperature. Yet in recent investigation, it has been shown that a manner in which the modelling accuracy can be enhanced is to increase the vertical thermal conductivity parameter k_z. Therefore, the objective for writing this report has been to investigate whether a valid physical reason exists for increasing k_z, or whether an increase of k_z effectively just acts as a cover for model imperfections. In pursuit of the correct answer to this question, a simplified model of heat dissipation, for which analytical solutions from previous works exist, was considered. The model is made up of a grid block derived from a layer-cake model comprised of an infinite series of two alternating layers with identical constant properties and dimensions, but different initial temperatures. In this research, the factor of increase in k_z that produces the highest attainable similarity of the grid block solution with the analytical solution has been calculated to investigate the discrepancy between solutions. Consequently, a technique called ‘superposition’ was applied to both the analytical and superposition solutions in an attempt to increase their similarity to the physical situation.

Results from the models described show that when the rate of heating is altered to be more realistic, the differences between the grid block and analytical solutions are significantly smaller than when using one single temperature increment. As elaborated in Cases 1 & 2, when temperature change takes place instantaneously, the optimal factor of increase of k_z so that the two different solutions are most similar has been found to be 4.1. However, raising the temperature gradually, as done in Cases 3 & 4, results in a much better resemblance between the grid block temperatures and the analytical temperature development. Results show that the lower the implemented rate of heating is, the more the results collected by running the model based on a finite-difference solution resemble the analytical results.

The temperature development of two fast-moving cold temperature layers was tracked in Section 4.5 using a thermal dispersion simulation, in an attempt to determine a realistic heating rate in actual geothermal doublets. At the heating rates that have been derived by tracking these two layers, the grid block solutions showed only insignificant deviations from the analytical solutions. The application of heating at these realistic rates resulted in most effectual factors of increase for k_z of 1.19 and 1.79. This suggests that there indeed might be a physically grounded reason to implement an increase in k_z., though the factor would be reasonably small. Nonetheless, implementing these factors of increase would only bring about minor changes when implemented in simulations and would not fully rectify the failure to quantitively fit the initial drop in produced water temperature.

Although this investigation has not found a physically justified reason for increasing the vertical thermal conductivity parameter k_z by any significant amount, this does not imply that there is none. The reason for this is that this research only investigated a much-simplified layer-cake model which bears limited resemblance to the thermal dispersion taking place in situ. On top of that, at a minimum slightly influential effects, including heat convection and thermal generation within the reservoir have not been accounted for. Therefore, further research into this issue is required to address the problem in all its complexities.

Literature

Bonté, Damien, J-D. Van Wees, and J. M. Verweij. "Subsurface temperature of the onshore Netherlands: new temperature dataset and modelling." *Netherlands Journal of Geosciences* 91.4 (2012): 491-515

Daniilidis, A., Nick, H. M., & Bruhn, D. F. (2020). Interdependencies between physical, design and operational parameters for direct use geothermal heat in faulted hydrothermal reservoirs. *Geothermics*, *86*, 101806. https://doi.org/10.1016/j.geothermics.2020.101806

Daniilidis, A., Nick, H. M., & Bruhn, D. F. (2021). Interference between geothermal doublets across a fault under subsurface uncertainty; implications for field development and regulation. *Geothermics*, *91*, 102041. https://doi.org/10.1016/j.geothermics.2021.102041

Dijkstra, H., Dinkelman, D., Hanegraaf, M., Veldkamp, H., & van Wees, J. D. (2020, December). *Duurzaamheid van geothermie in warmtenetten*. TNO, Petten. https://repository.tno.nl//islandora/object/uuid:a3c8e196-06e7-4444-83d0-312adc641073

EBN. (2018, May). *Master Plan Geothermal Energy in the Netherlands*. EBN DAGO Stichting Platform Geothermie Stichting Warmtenetwerk. https://kennisbank.ebn.nl/het-masterplan-aardwarmte-nederland/

Hammingh, P., Daniels, B., Koutstaal, P., Schure, K., & Hekkenberg, M. (2020, October 29). *Klimaat- en Energieverkenning 2020*. PBL Planbureau voor de Leefomgeving. Retrieved 9 June 2022, from https://www.pbl.nl/publicaties/klimaat-en-energieverkenning-2020

de Hoop, S., Voskov, D., & Bertotti, G. (2019). Uncertainty Quantification and History Matching for Naturally Fractured Carbonate Reservoirs. *Third EAGE WIPIC Workshop: Reservoir Management in Carbonates*. https://doi.org/10.3997/2214-4609.201903106

Mahbaz, S. B., Yaghoubi, A., Dehghani-Sanij, A., Sarvaramini, E., Leonenko, Y., & Dusseault, M. B. (2021). Well-Doublets: A First-Order Assessment of Geothermal SedHeat Systems. *Applied Sciences*, *11*(2), 697. https://doi.org/10.3390/app11020697

Mijnlieff, H. F. (2020). Introduction to the geothermal play and reservoir geology of the Netherlands. *Netherlands Journal of Geosciences*, *99*. https://doi.org/10.1017/njg.2020.2

Milieu Centraal. (2020). *Aardwarmte: duurzame warmte uit de grond*. Retrieved 9 June 2022, from https://www.milieucentraal.nl/klimaat-en-aarde/energiebronnen/aardwarmte/

Ohio University. (2015). *Insulated Boundary Conditions*. Ohiouniversityfaculty. Retrieved 9 June 2022, from https://www.studocu.com/en-us/document/ohio-university/applied-numerical-methods/lecture-38-math-3600-spring-2015/874573

Tang, J., Wang, Y., & Rossen, W. R. (2021). *On an Analytical Model for Thermal Taylor Dispersion in Layered Porous Media*.

University of Ottowa. (2007, February 1). *Heat Conduction*. Booksite.Elsevier.Com. Retrieved 9 June 2022, from https://www.coursehero.com/file/26038056/9780123735881pdf/

Wang, Y., Voskov, D., Khait, M., Saeid, S., & Bruhn, D. (2021). Influential factors on the development of a low-enthalpy geothermal reservoir: A sensitivity study of a realistic field. *Renewable Energy*, *179*, 641–651. https://doi.org/10.1016/j.renene.2021.07.017

Watson, R., McCarthy, J. J., Canziani, P., Nakcenovic, N., & Hisas, L. (2019, November). *The Truth Behind the Climate Pledges* (No. 978-0-9831909-3–6).

Wu, S. (2010). Heat energy storage and cooling in buildings. In Materials for Energy Efficiency and Thermal Comfort in Buildings (pp. 101-126). Woodhead Publishing.

Zaal, C., Daniilidis, A., & Vossepoel, F. C. (2021). Economic and fault stability analysis of geothermal field development in direct-use hydrothermal reservoirs. *Geothermal Energy*, *9*(1). https://doi.org/10.1186/s40517-021-00193-0

Appendix 1 – Tables

Time Step	$\tau_1 = 0.025$	$\tau_{1,Converted\ Data\ Companion}$	θ_{Top}	θ^*_{Top}	$\theta_{Average}$	$\theta^*_{Average}$

0	0	0	1	0	1	0
τ_1	0.025	0.00625	1	0	0.86	0.14
$2\tau_1$	0.05	0.0125	1	0	0.76	0.24
$3\tau_1$	0.075	0.01875	0.97	0.03	0.68	0.32
$4\tau_1$	0.1	0.025	0.95	0.05	0.64	0.36
$5\tau_1$	0.125	0.03125	0.91	0.09	0.6	0.4
$6\tau_1$	0.15	0.0375	0.89	0.11	0.56	0.44
$7\tau_1$	0.175	0.04375	0.85	0.15	0.53	0.47
$8\tau_1$	0.2	0.05	0.80	0.20	0.49	0.51
$9\tau_1$	0.225	0.05625	0.77	0.23	0.467	0.533
$10\tau_1$	0.25	0.0625	0.72	0.28	0.44	0.56

Table 1. Dimensionless temperature values at different times for $\tau_1 = \frac{\alpha t_1}{H^2} = 0.025$, *from Transport Phenomena Data Companion (Janssen & Warmoeskerken, 1987)*

Time Step	$\tau_1 = 0.05$	$\tau_{1,Converted\ Data\ Companion}$	θ_{Top}	θ^*_{Top}	$\theta_{Average}$	$\theta^*_{Average}$
0	0	0	1	0	1	0
τ_1	0.05	0.0125	1	0	0.76	0.24
$2\tau_1$	0.1	0.025	0.95	0.05	0.64	0.36
$3\tau_1$	0.15	0.0375	0.89	0.11	0.56	0.44
$4\tau_1$	0.2	0.05	0.80	0.20	0.49	0.51
$5\tau_1$	0.25	0.0625	0.72	0.28	0.44	0.56
$6\tau_1$	0.3	0.075	0.63	0.37	0.39	0.61
$7\tau_1$	0.35	0.0875	0.56	0.44	0.35	0.65

Table 2. Dimensionless temperature values at different times for $\tau_1 = \frac{\alpha t_1}{H^2} = 0.05,$ *from Transport Phenomena Data Companion (Janssen & Warmoeskerken, 1987)*

Time Step	$\tau_1 = 0.1$	$\tau_{1,Converted\ Data\ Companion}$	θ_{Top}	θ^*_{Top}	$\theta_{Average}$	$\theta^*_{Average}$
0	0	0	1	0	1	0
τ_1	0.1	0.025	0.95	0.05	0.64	0.36
$2\tau_1$	0.2	0.05	0.80	0.20	0.49	0.51
$3\tau_1$	0.3	0.075	0.63	0.37	0.38	0.62
$4\tau_1$	0.4	0.1	0.49	0.51	0.31	0.69
$5\tau_1$	0.5	0.125	0.44	0.56	0.27	0.73

Table 3. Dimensionless temperature values at different times for $\tau_1 = \frac{\alpha t_1}{H^2} = 0.1,$ *from Transport Phenomena Data Companion (Janssen & Warmoeskerken, 1987)*

Time Step	$\tau_1 = 0.2$	$\tau_{1,Converted\ Data\ Companion}$	θ_{Top}	θ^*_{Top}	$\theta_{Average}$	$\theta^*_{Average}$
0	0	0	1	0	1	0
τ_1	0.2	0.05	0.80	0.20	0.49	0.51
$2\tau_1$	0.4	0.1	0.49	0.51	0.31	0.69
$3\tau_1$	0.6	0.15	0.29	0.71	0.187	0.813
$4\tau_1$	0.8	0.2	0.20	0.80	0.116	0.884

Table 4. Dimensionless temperature values at different times for $\tau_1 = \frac{\alpha t_1}{H^2} = 0.2,$ *from Transport Phenomena Data Companion (Janssen & Warmoeskerken, 1987)*

Time Step	$\tau_1 = 0.4$	$\tau_{1,Converted\ Data\ Companion}$	θ_{Top}	θ^*_{Top}	$\theta_{Average}$	$\theta^*_{Average}$
0	0	0	1	0	1	0
$0.1\tau_1$	0.04	0.01	1	0	0.77	0.23
$0.2\tau_1$	0.08	0.02	0.97	0.03	0.67	0.33

$0.3\tau_1$	0.12	0.03	0.94	0.06	0.60	0.40
$0.4\tau_1$	0.16	0.04	0.86	0.14	0.54	0.46
$0.6\tau_1$	0.24	0.06	0.74	0.26	0.44	0.56
$0.8\tau_1$	0.32	0.08	0.60	0.4	0.36	0.64
τ_1	0.4	0.1	0.49	0.51	0.31	0.69
$1.2\tau_1$	0.48	0.12	0.45	0.55	0.25	0.75
$1.4\tau_1$	0.56	0.14	0.40	0.6	0.20	0.8
$1.6\tau_1$	0.64	0.16	0.37	0.63	0.172	0.828
$1.8\tau_1$	0.72	0.18	0.34	0.66	0.144	0.856
$2\tau_1$	0.8	0.2	0.19	0.81	0.116	0.884
$3\tau_1$	1.2	0.3	0.067	0.933	0.042	0.958
$4\tau_1$	1.6	0.4	0.026	0.974	0.017	0.983

Table 5. Dimensionless temperature values at different times for $\tau_1 = \frac{\alpha t_1}{H^2} = 0.4,$ *from Transport Phenomena Data Companion (Janssen & Warmoeskerken, 1987)*

Time Step	$\tau_1 = 0.8$	$\tau_{1,Converted\ Data\ Companion}$	θ_{Top}	θ^*_{Top}	$\theta_{Average}$	$\theta^*_{Average}$
0	0	0	1	0	1	0
τ_1	0.8	0.2	0.19	0.81	0.154	0.846
$2\tau_1$	1.6	0.4	0.067	0.933	0.017	0.983
$3\tau_1$	2.4	0.6	0	1	0	1
$4\tau_1$	3.2	0.8	0	1	0	1

Table 6. Dimensionless temperature values at different times for $\tau_1 = \frac{\alpha t_1}{H^2} = 0.8,$ *from Transport Phenomena Data Companion (Janssen & Warmoeskerken, 1987)*

Time Step	$\tau_1 = 1.35$	$\tau_{1,Converted\ Data\ Companion}$	θ_{Top}	θ^*_{Top}	$\theta_{Average}$	$\theta^*_{Average}$
0	0	0	1	0	1	0
$0.1\tau_1$	0.135	0.0338	0.89	0.11	0.582	0.418
$0.2\tau_1$	0.27	0.065	0.69	0.31	0.416	0.584
$0.3\tau_1$	0.405	0.1013	0.49	0.51	0.31	0.69
$0.4\tau_1$	0.54	0.135	0.37	0.63	0.218	0.782
$0.6\tau_1$	0.81	0.203	0.19	0.81	0.154	0.846
$0.8\tau_1$	1.08	0.27	0.097	0.903	0.056	0.944
τ_1	1.35	0.338	0.046	0.954	0.028	0.972
$1.2\tau_1$	1.62	0.405	0.026	0.974	0.016	0.984
$1.4\tau_1$	1.89	0.4725	0.01	0.99	0	1
$1.6\tau_1$	2.16	0.54	0	1	0	1
$1.8\tau_1$	2.43	0.608	0	1	0	1
$2\tau_1$	2.7	0.675	0	1	0	1
$3\tau_1$	4.05	1.0125	0	1	0	1
$4\tau_1$	5.4	1.35	0	1	0	1

Table 7. Dimensionless temperature values at different times for $\tau_1 = \frac{\alpha t_1}{H^2} = 1.35$, *from Transport Phenomena Data Companion (Janssen & Warmoeskerken, 1987)*

Time Step	$\tau_1 = 1.6$	$\tau_{1,Converted\ Data\ Companion}$	θ_{Top}	θ^*_{Top}	$\theta_{Average}$	$\theta^*_{Average}$
0	0	0	1	0	1	0
τ_1	1.6	0.4	0.026	0.974	0.017	0.983

$2\tau_1$	3.2	0.8	0	1	0	1
$3\tau_1$	6.4	1.2	0	1	0	1
$4\tau_1$	12.8	2.4	0	1	0	1

Table 8. Dimensionless temperature values at different times for $\tau_1 = \frac{\alpha t_1}{H^2} = 1.6,$ *from Transport Phenomena Data Companion (Janssen & Warmoeskerken, 1987)*

Time Step	$\tau_1 = 2$	$\tau_{1,Converted\ Data\ Companion}$	θ_{Top}	θ^*_{Top}	$\theta_{Average}$	$\theta^*_{Average}$
0	0	0	1	0	1	0
τ_1	2	0.5	0.009	0.991	0.006	0.994
$2\tau_1$	4	1	0	1	0	1
$3\tau_1$	6	1.5	0	1	0	1
$4\tau_1$	8	2	0	1	0	1

Table 9. Dimensionless temperature values at different times for $\tau_1 = \frac{\alpha t_1}{H^2} = 2,$ *from Transport Phenomena Data Companion (Janssen & Warmoeskerken, 1987)*

Time Step	$\tau_1 = 4$	$\tau_{1,Converted\ Data\ Companion}$	θ_{Top}	θ^*_{Top}	$\theta_{Average}$	$\theta^*_{Average}$
0	0	0	1	0	1	0
τ_1	4	1	0.009	0.991	0.006	0.994
$2\tau_1$	8	2	0	1	0	1
$3\tau_1$	12	3	0	1	0	1
$4\tau_1$	16	4	0	1	0	1

Table 10. Dimensionless temperature values at different times for $\tau_1 = \frac{\alpha t_1}{H^2} = 4,$ *from Transport Phenomena Data Companion (Janssen & Warmoeskerken, 1987)*

Appendix 2- Semi Log Plots

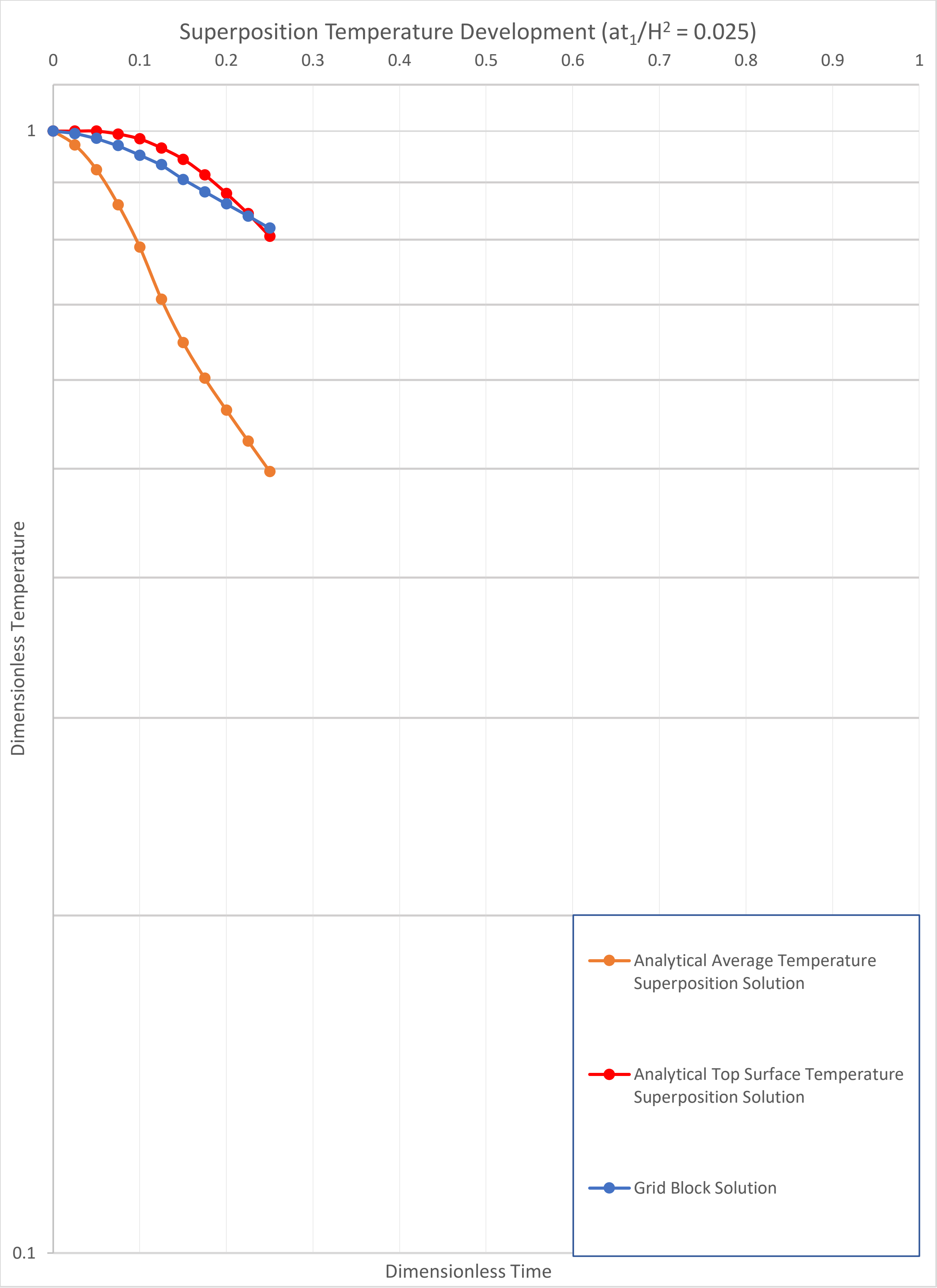

Figure 16. A plot that compares modelled superposition results with temperature increments at a heating interval of $\tau_1 = \frac{\alpha t_1}{b^2} = 0.025$ *against the analytical solution from Transport Phenomena Data Companion*

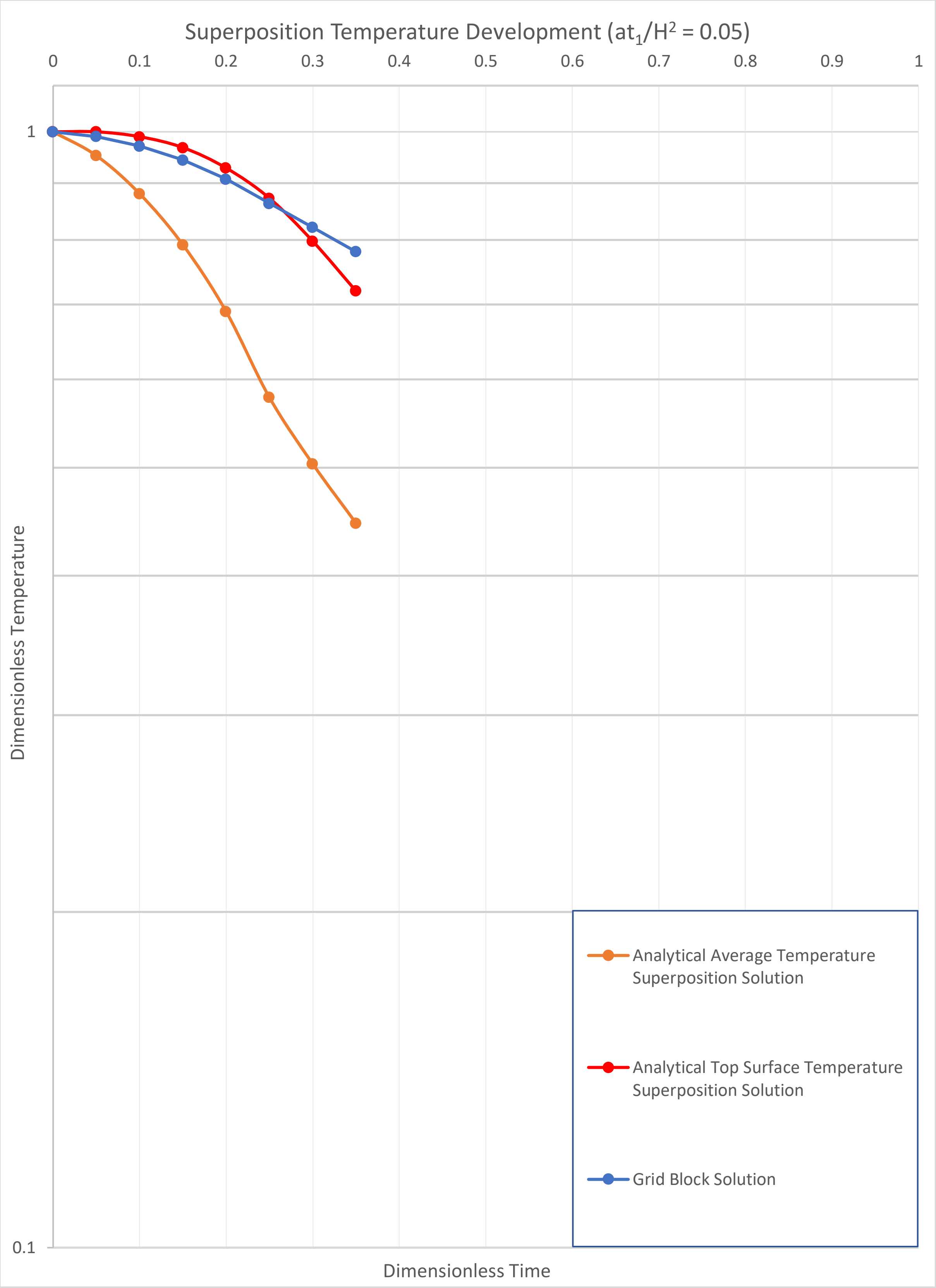

Figure 17. A plot that compares modelled superposition results with temperature increments at a heating interval of $\tau_1 = \frac{\alpha t_1}{b^2} = 0.05$ *against the analytical solution from Transport Phenomena Data Companion*

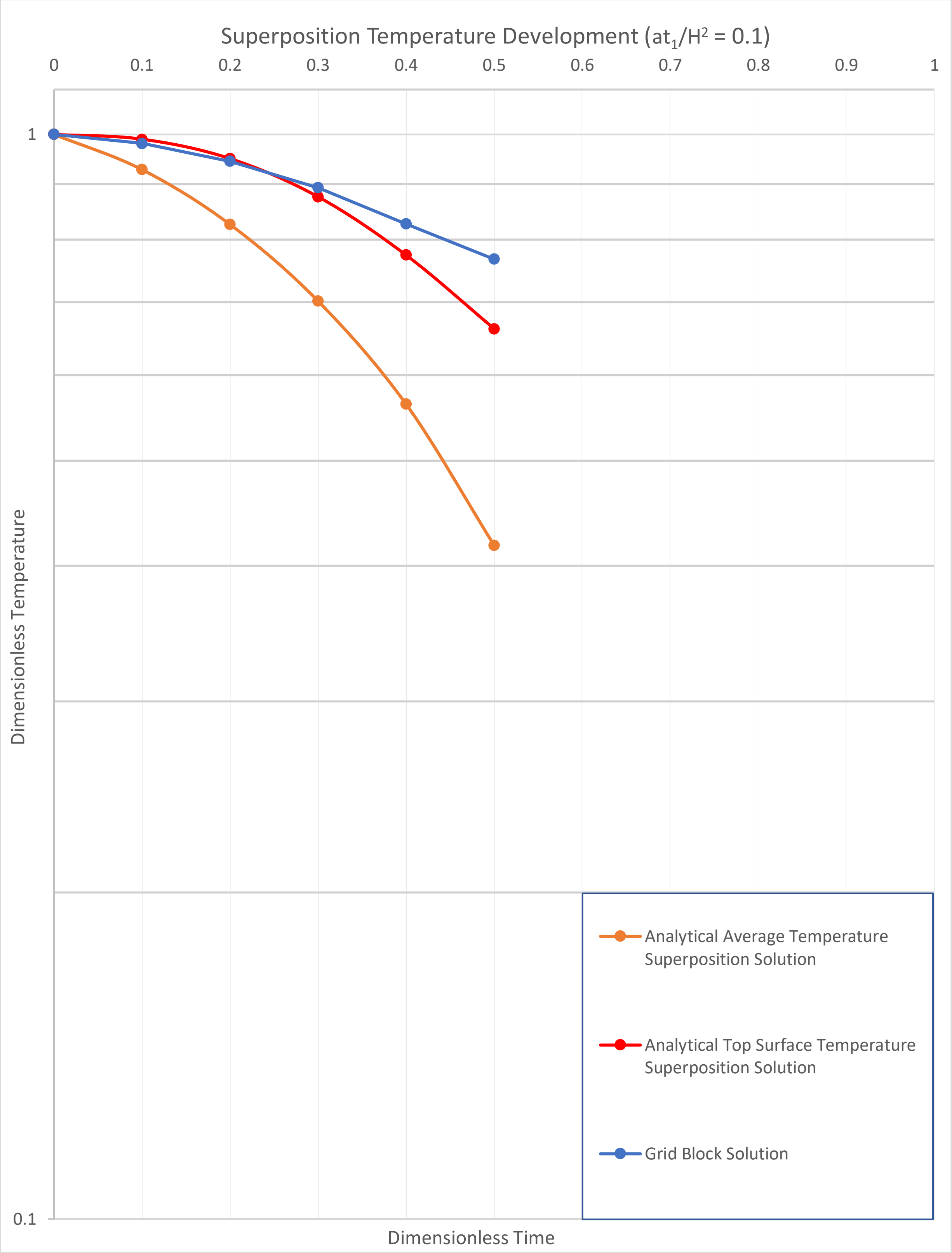

Figure 18. A plot that compares modelled superposition results with temperature increments at a heating interval of $\tau_1 = \frac{\alpha t_1}{b^2} = 0.1$ *against the analytical solution from Transport Phenomena Data Companion*

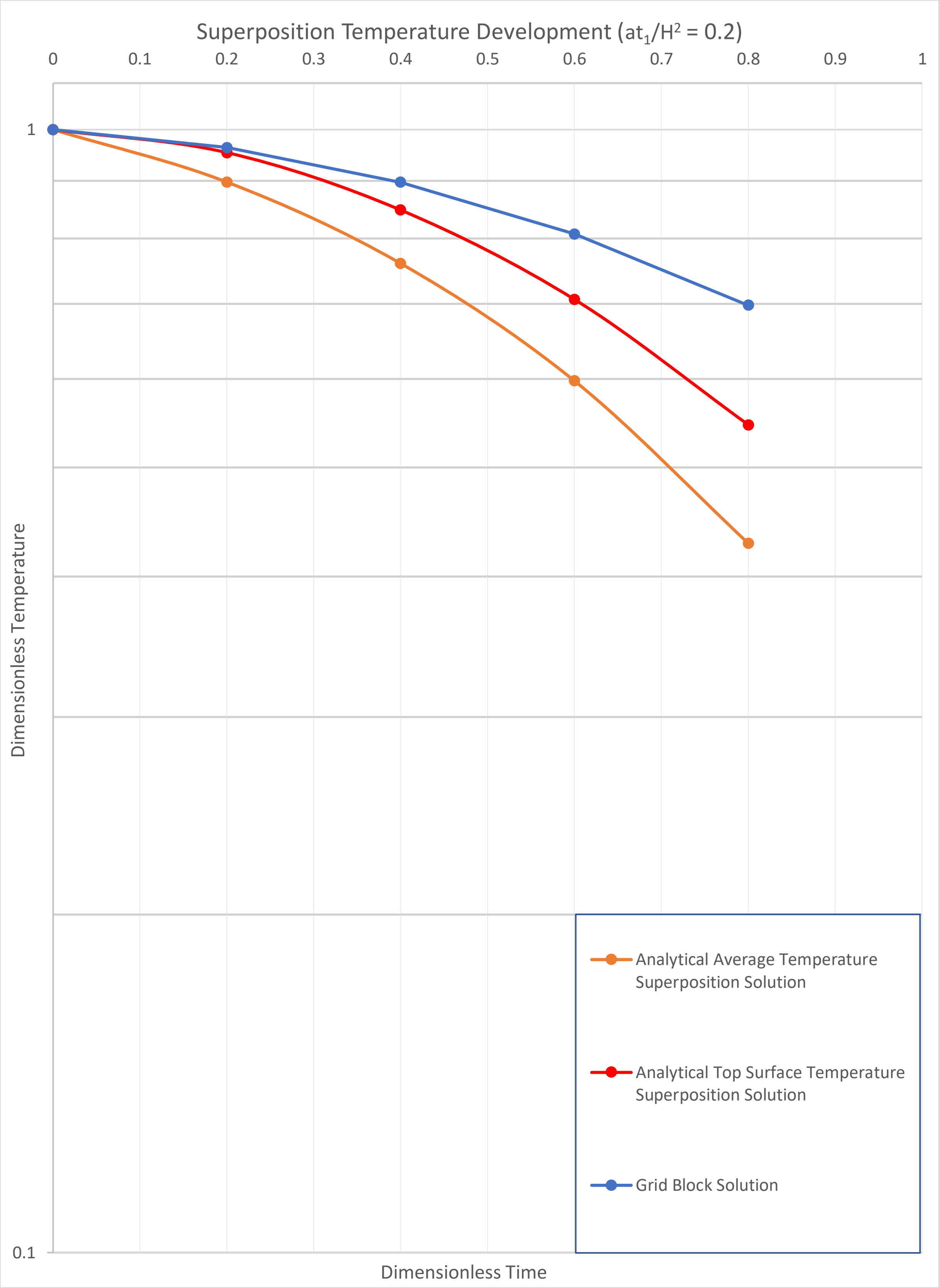

Figure 19. A plot that compares modelled superposition results with temperature increments at a heating interval of $\tau_1 = \frac{\alpha t_1}{b^2} = 0.2$ *against the analytical solution from Transport Phenomena Data Companion*

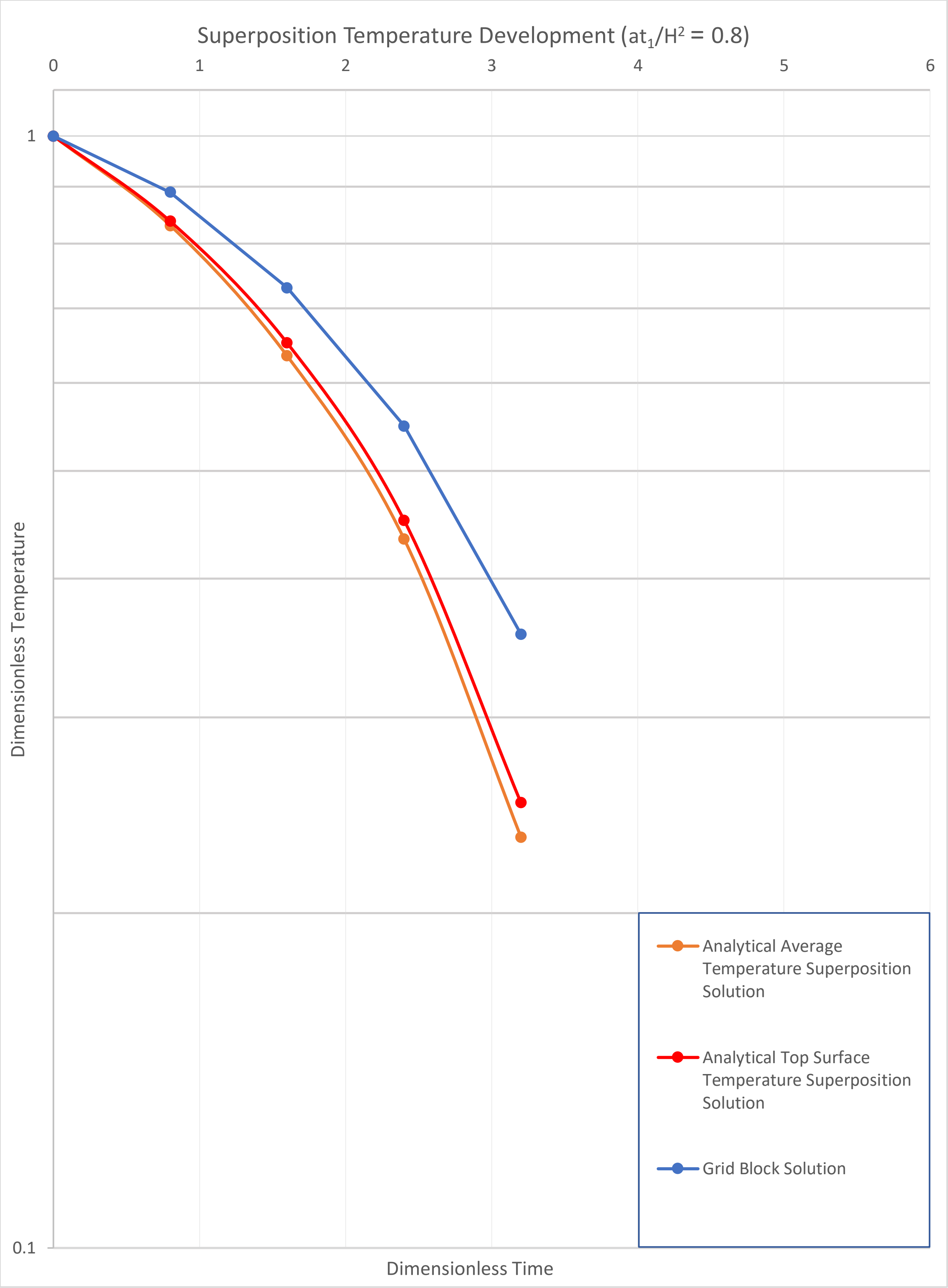

Figure 20. A plot that compares modelled superposition results with temperature increments at a heating interval of $\tau_1 = \frac{\alpha t_1}{b^2} = 0.8$ *against the analytical solution from Transport Phenomena Data Companion*

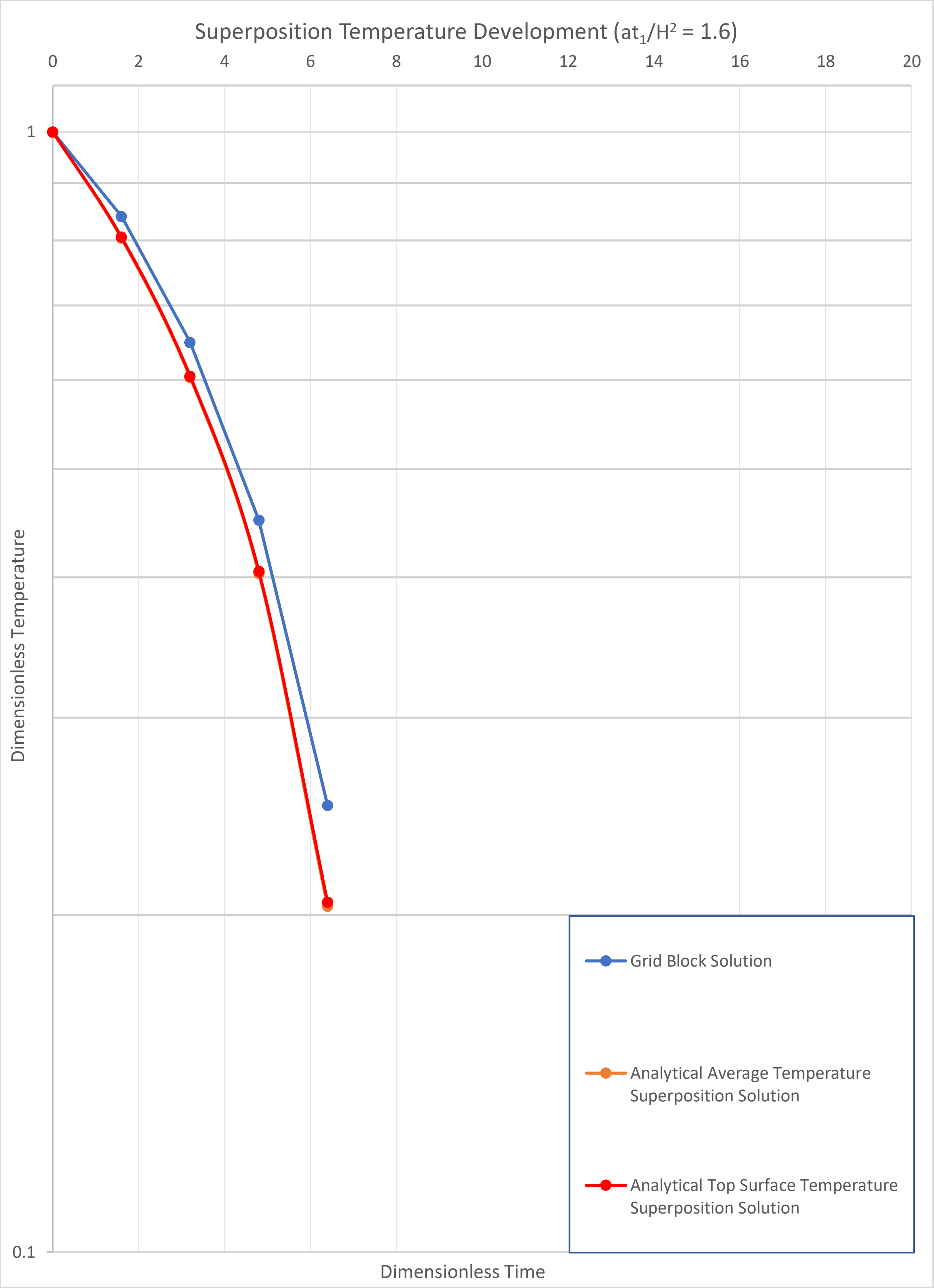

Figure 21. A plot that compares modelled superposition results with temperature increments at a heating interval of $\tau_1 = \frac{\alpha t_1}{b^2} = 1.6$ *against the analytical solution from Transport Phenomena Data Companion*

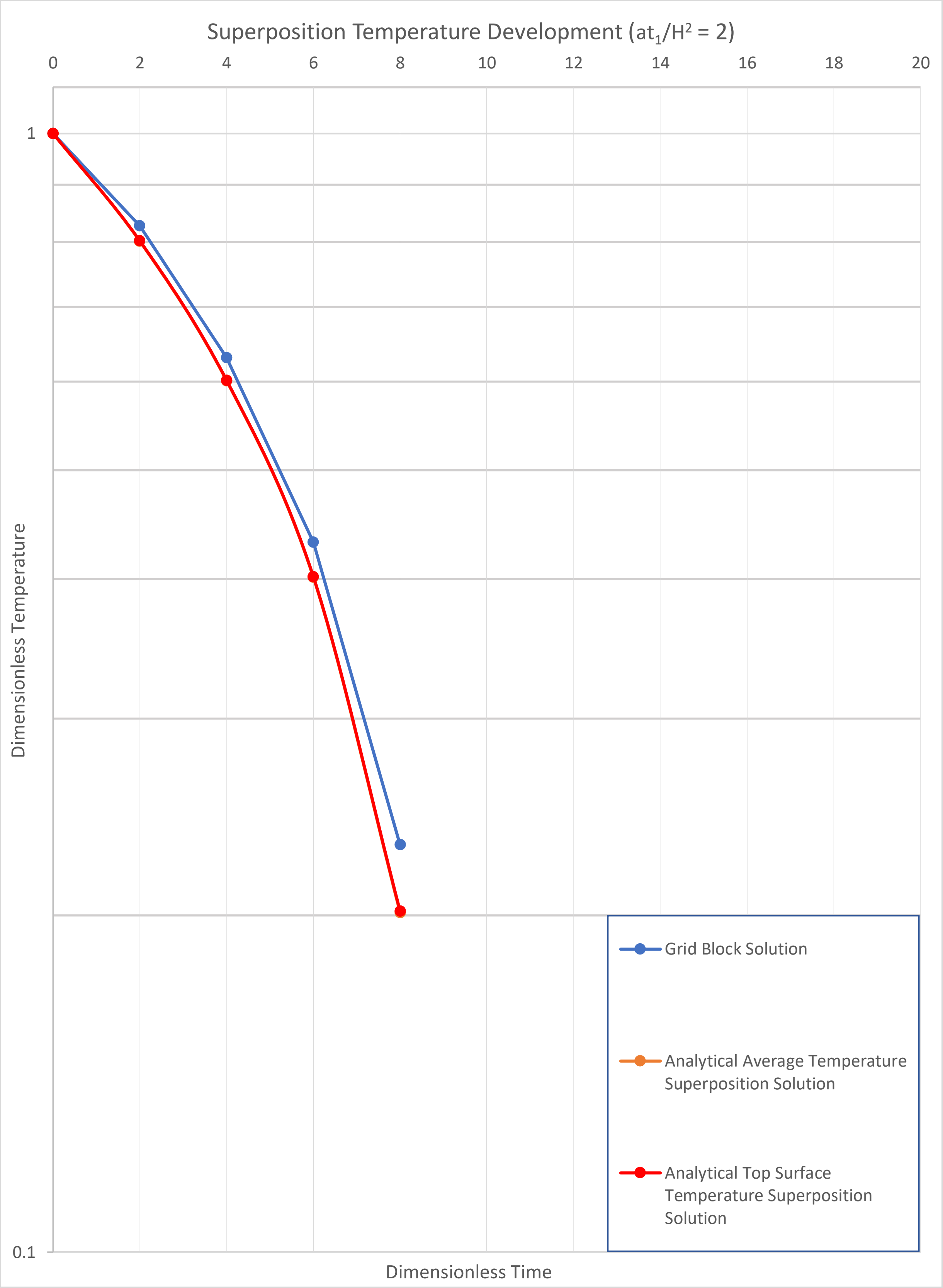

Figure 22. A plot that compares modelled superposition results with temperature increments at a heating interval of $\tau_1 = \frac{\alpha t_1}{b^2} = 2$ *against the analytical solution from Transport Phenomena Data Companion*

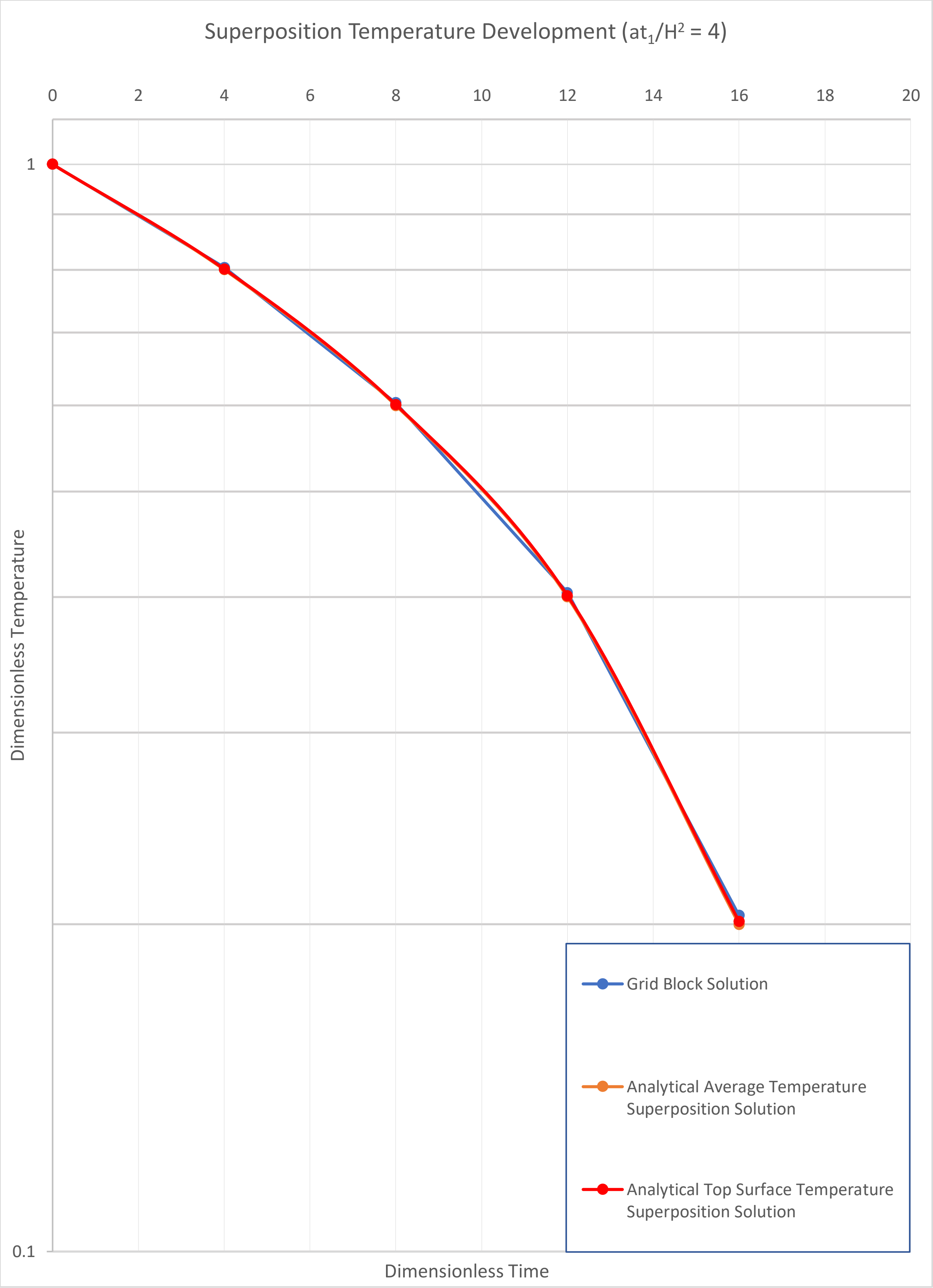

Figure 23. A plot that compares modelled superposition results with temperature increments at a heating interval of $\tau_1 = \frac{at_1}{b^2} = 4$ *against the analytical solution from Transport Phenomena Data Companion*